ISTANBUL TECHNICAL UNIVERSITY ★ GRADUATE SCHOOL

IN-SITU MECHANICAL TESTING AND DIGITAL IMAGE CORRELATION OF SUPER DUPLEX STAINLESS STEELS TO UNDERSTAND HYDROGEN EMBRITTLEMENT

M.Sc. THESIS

Bilgehan Murat ŞEŞEN

Department of Material Science and Engineering

Material Science and Engineering Programme

AUGUST 2022

ISTANBUL TECHNICAL UNIVERSITY ★ GRADUATE SCHOOL

IN-SITU MECHANICAL TESTING AND DIGITAL IMAGE CORRELATION OF SUPER DUPLEX STAINLESS STEELS TO UNDERSTAND HYDROGEN EMBRITTLEMENT

M.Sc. THESIS

Bilgehan Murat ŞEŞEN
(521201004)

Department of Material Science and Engineering

Material Science and Engineering Programme

Thesis Advisor: Assist. Prof. Dr. Cem ÖRNEK

AUGUST 2022

İSTANBUL TEKNİK ÜNİVERSİTESİ ★ LİSANSÜSTÜ EĞİTİM ENSTİTÜSÜ

SÜPER DUPLEKS PASLANMAZ ÇELİKLERİN HİDROJEN GEVREKLİĞİNİ ANLAMAK İÇİN YERİNDE MEKANİK TEST VE DİJİTAL GÖRÜNTÜ KORELASYONU

YÜKSEK LİSANS TEZİ

Bilgehan Murat ŞEŞEN
(521201004)

Malzeme Bilimi ve Mühendisliği Anabilim Dalı

Malzeme Bilimi ve Mühendisliği Programı

Tez Danışmanı: Dr. Öğr. Üyesi Cem ÖRNEK

AĞUSTOS 2022

Bilgehan Murat ŞEŞEN, a M.Sc. student of ITU Graduate School student ID 521201004, successfully defended the thesis/dissertation entitled "IN-SITU MECHANICAL TESTING AND DIGITAL IMAGE CORRELATION OF SUPUER DUPLEX STAINLESS STEEL TO UNDERSTAND HYDROGEN EMBRITTLEMENT", which he prepared after fulfilling the requirements specified in the associated legislations, before the jury whose signatures are below.

Thesis Advisor :	**Assist. Prof. Dr. Cem ÖRNEK** Istanbul Technical University	.....
Jury Members :	**Assist. Prof. Dr. Cem ÖRNEK** Istanbul Technical University	.....
	Prof. Dr. Murat BAYDOĞAN Istanbul Technical University	.....
	Assoc. Prof. Dr. Savaş DİLİBAL Istanbul Gedik University	.....

Date of Submission : 12 August 2022
Date of Defense : 24 August 2022

To my beloved family,

FOREWORD

I would like to thank my esteemed dear advisor, Assist. Prof. Dr. Cem ÖRNEK, who provided me with unique opportunities throughout my studies, always thought of the next step for his student, never spared his support and was an idol for me.

I would like to thank Prof. Dr. Mustafa ÜRGEN, Prof. Dr. Kürşat KAZMANLI, and Assist. Prof. Dr. Nuri SOLAK, who had great efforts on me and did not spare their criticism, suggestions and help.

I would like to thank Prof. Dr. Murat BAYDOĞAN, who made me love material science and engineering.

I would like to thank Dr. Çağatay YELKARASI, who was an older brother to me, who solved all my problems and guided me, who helped me constantly, whom I could consult and talk about anything. I learned a lot from him during my thesis process, how to think and how to solve a problem. I cannot thank my brother enough, whose intelligence and knowledge I admire. Furthermore, a special thanks to Perim YELKARASI.

I would like to thank Res. Assis. Burçak AVCI, who was an older sister to me, who thought of the worst possible scenario and thought the best for you. I can't thank enough my dear sister who called me and sat me down to write my thesis while I was avoiding, for the coffees and conversations we had at 7 am.

I would like to thank Res. Assis. Göksel HIZLI, who was an older brother to me, with whom I have worked since undergraduate and whose support I always felt.

I would like to thank the surface and corrosion group and especially for dear Dr. Erkan KAÇAR, Cihan ERDEM, Dilan ER, Seyhan ATİK, Dr. Eren SEÇKİN, Güney AKDAŞ, Pınar AFŞİN, and Dr. Selim ERTÜRK.

I would like to thank my dear friends Sergen Halim AYHAN, Ege DEMİR, Res. Assis. Kerem DİZDAR, Res. Assis. Atakan Ege SAVAŞ, Nuri PALAMUTÇU, Res. Assis. Semih ATEŞ, Taha ÖZKAYHAN, and my first friend from ITU, Kamer ERDOĞAN, whose support and friendship I will never forget during my master's degree.

I would like to thank my high school friends Erkin ERGEZEN and Emre GÜRTÜRK (Yabo) who took me to the Gebze and brought me.

I would like to thank my dear friends Kaan ÖZSARAÇ and Betül TEKİN, who contributed a lot to my thesis, for their help.

I would like to thank my dear friend Res. Assis. Beste PAYAM, who helped me throughout this process, whose support I always felt, who saw and knew everything, and who is my ace boom-boom. I can't thank enough my dear twin, with whom I compete in everything, give the same reactions at the same time, laugh and have fun with her all the time.

I would like to thank my lovely dear friend Ezgi HATİPOĞLU, who was always there for me and always thought of me. I can't thank enough my lovely friend, who was more nervous and excited for me than me. It would have been very difficult to achieve these without her.

I would like to thank to The Scientific and Technological Research Council of Turkey (TUBITAK) for the International Fellowship for Outstanding Researcher (2232) scholarship programme under contract number 118C227, which supported me during my M.Sc. thesis.

Finally, I would like to thank my beloved family for everything they have always supported and stood by my side.

August 2022

Bilgehan Murat ŞEŞEN
(Metallurgical and Materials Engineer)

TABLE OF CONTENTS

Page

FOREWORD ..... **ix**
TABLE OF CONTENTS ..... **xi**
ABBREVIATIONS ..... **xiii**
SYMBOLS ..... **xv**
LIST OF TABLES ..... **xvii**
LIST OF FIGURES ..... **xix**
SUMMARY ..... **xxi**
ÖZET ..... **xxiii**
1. INTRODUCTION **1**
2. MOTIVATION AND AIM OF RESEARCH **3**
3. SCOPE OF RESEARCH **5**
4. LITERATURE REVIEW **7**
4.1 Hydrogen Embrittlement Mechanisms 8
4.1.1 Hydrogen-enhanced decohesion (HEDE) 8
4.1.2 Hydrogen-enhanced localized plasticity (HELP) 9
4.1.3 Adsorption-induced dislocation emission (AIDE) 9
4.1.4 Hydride formation 10
4.1.5 Hydrogen-enhanced strain-induced vacancies (HESIV) 10
4.1.6 The defactant concept 11
4.2 Super Duplex Stainless Steel 11
4.3 Deformation of Metals 12
4.4 State-of-the-art Testing for Hydrogen Embrittlement 15
4.5 Hydrogen Absorption 19
4.6 Hydrogen Diffusion 20
5. CHARACTERIZATION TECHNIQUES/TOOLS USED **23**
5.1 Metallography 23
5.2 Micro-Mechanical Testing (DEBEN) 23
5.3 Digital Optical Microscope (HIROX) 24
5.4 Digital Image Correlation 24
6. EXPERIMENTAL PROCEDURE **29**
6.1 Material Investigated 29
6.2 Microstructure Characterization 29
6.3 Electrochemical Hydrogen Charging 30
6.4 In-situ Micro-tensile Testing of Pre-Hydrogen Charged Specimens 31
6.5 Digital Image Correlation 32

6.6 In-situ Micro-tensile Testing during Hydrogen Charging 33
6.7 Fractography 36
7. RESULTS 37
7.1 Microstructure 37
7.2 Effect of Absorbed Hydrogen on the Deformation Behavior 38
7.2.1 Stress-strain curves 38
7.2.2 Deformation characteristics 39
7.2.3 Fracture morphology 41
7.3 Effect of Deformation during Hydrogen Charging 42
7.4 Digital Image Correlation 45
8. DISCUSSION 51
9. CONCLUSION 55
10. FUTURE WORKS 57
REFERENCES 59
CURRICULUM VITAE 63

ABBREVIATIONS

SDSS	**:** Super duplex stainless steels
DIC	**:** Digital image correlation
ppm	**:** parts-per-million
HEDE	**:** Hydrogen enhanced decohesion
HELP	**:** Hydrogen enhanced localized plasticity
AIDE	**:** Adsorption induced dislocation emission
HESIV	**:** Hydrogen enhanced strain induced vacancies
TEM	**:** Transmission electron microscopy
TDS	**:** Thermal desorption spectrometry
Surfactants	**:** Surface active agent
Defactant	**:** Defect active agent
PRE	**:** Pitting resistance equivalent
bcc	**:** body-centered cubic
fcc	**:** face-centered cubic
APF	**:** Atomic packing factor
APT	**:** Atom probe tomography
SIMS	**:** Secondary ion mass spectrometr
SSRT	**:** Slow strain rate testing
SEM	**:** Scanning electron microscope
ECCI	**:** Electron channeling contrast imaging
EDM	**:** Electric discharge machining
PLA	**:** Polylactic acid
PEEK	**:** Polyether ether ketone
SKPFM	**:** Scanning kelvin probe force microscopy
EBSD	**:** Electron backscatter diffraction

SYMBOLS

CO_2	**:** Carbon dioxide
Cr	**:** Chromium
Ni	**:** Nickel
µm	**:** Micrometer
mm	**:** Millimeter
°C	**:** Celsius
$\boldsymbol{\Gamma}$	**:** Ratio of the amount of defactant atoms and the defect density
$\boldsymbol{V}$	**:** Volume
$\boldsymbol{n_B}$	**:** Number of solvent atoms
$\boldsymbol{n_H}$	**:** Number of hydrogen atoms
$\boldsymbol{T}$	**:** Temperature
$\boldsymbol{\mu}$	**:** Chemical potential
E	**:** Modulus of elasticity
σ	**:** Engineering stress
e	**:** Engineering strain
$\boldsymbol{\tau}$	**:** Peierls stress
$\boldsymbol{G}$	**:** Shear modulus
$\boldsymbol{e}$	**:** Exponential
$\boldsymbol{\pi}$	**:** Pi number
$\boldsymbol{w}$	**:** Dislocation width
$\boldsymbol{b}$	**:** Burgers vector
s	**:** Second
$\boldsymbol{H^+_{(aq)}}$	**:** Hydrogen ion in aqueous solution
$\boldsymbol{e^-_{(M)}}$	**:** Electron in metal
$\boldsymbol{H}$	**:** Absorbed hydrogen
$\boldsymbol{H_2O_{(l)}}$	**:** Water
$\boldsymbol{OH^-_{(aq)}}$	**:** Hydroxide ion in aqueous solution
%	**:** Percent
SiC	**:** Silicon carbide

V	**:** Voltage
min	**:** Minute
kN	**:** Kilonewton
x*, y*	**:** Positions of the new subset after the deformation
$\mathbf{u_x}$**,** $\mathbf{u_y}$	**:** Displacements
Δx, Δy	**:** Distance along axis
$\boldsymbol{\partial}$	**:** Partial derivative
$\frac{\partial u_x}{\partial x}, \frac{\partial u_y}{\partial y}, \frac{\partial u_y}{\partial x}, \frac{\partial u_x}{\partial y}$	**:** Displacement gradients
$\mathbf{E_{xx}}$**,** $\mathbf{E_{yy}}$**,** $\mathbf{E_{xy}}$	**:** Strain along axis
wt.	**:** Weight
C	**:** Carbon
Si	**:** Silicon
Mn	**:** Manganese
P	**:** Phosphorus
S	**:** Sulfur
Mo	**:** Molybdenum
N	**:** Nitrogen
Cu	**:** Copper
Fe	**:** Iron
3D	**:** Three dimensional
mL	**:** Milliliter
M	**:** Molar
NaCl	**:** Sodium Chloride
mA	**:** Milliampere
cm	**:** Centimeter
N	**:** Newton
2D	**:** Two-dimensional
M	**:** Meter
$\boldsymbol{D_\delta}$	**:** Diffusion coefficient of ferrite
$\boldsymbol{D_\gamma}$	**:** Diffusion coefficient of austenite
x	**:** Distance
$\boldsymbol{D}$	**:** Diffusion coefficient
t	**:** Time

LIST OF TABLES

Page

Table 4.1 : Slip plane, direction and number of slip systems of crystal structures [26]. **15**
Table 6.1 : Chemical composition (in weight percent) of the investigated SDSSs. . **29**
Table 6.2 : Field of view and resolution information of the images taken with the HIROX digital microscope..... **30**
Table 6.3 : Experimental conditions of in-situ micro-tensile testing of hydrogen pre-charged specimens..... **31**
Table 6.4 : Experimental conditions for the in-situ micro-tensile tests with in-situ hydrogen charging. **35**

LIST OF FIGURES

Page

Figure 4.1 : Schematic representation of the HELP mechanism [5]..... **9**
Figure 4.2 : Schematic representation of the AIDE mechanism [5]. **10**
Figure 4.3 : Schematic representation of the hydride formation and fracture mechanism [5]..... **10**
Figure 4.4 : Schematic representations of bcc unit cell [26]..... **14**
Figure 4.5 : Schematic representations of fcc unit cell [26]. **14**
Figure 4.6 : Schematic representation of in-situ experimental setup [32]. **17**
Figure 4.7 : Schematic representation of an in-situ experimental setup for hydrogen charging [33]..... **18**
Figure 4.8 : Schematic experimental setup to investigate hydrogen desorption effects on dislocation mobility [34]..... **19**
Figure 4.9 : Schematic illustration shows the gas-phase hydrogen absorption process into the bulk material and the resulting embryonic stage of the HEDE mechanism of hydrogen embrittlement [35]..... **19**
Figure 5.1 : Images of the (a) in-situ tensile test experiment with digital optical microscope and tester and (b) magnified view of the miniature-sized DEBEN tester. **23**
Figure 5.2 : Computation of displacement of deformed subset via DIC [45]..... **25**
Figure 6.1 : Schematic representation of experimental setup for in-situ micro-tensile testing of hydrogen pre-charged specimens and processing of micrographs with DIC. **32**
Figure 6.2 : Schematic representation of (a) experimental setup for in-situ micro-tensile testing during hydrogen charging, (b) magnified view of (a), and (c) the 3D-printed electrochemical cell design. **33**
Figure 6.3 : Mounted specimens in (a) additively manufactured and (b) glass electrochemical cells sealed with fast drying silicon. The tensile specimen is 50 mm long. **34**
Figure 6.4 : Schematic representation of (a) experimental setup for in-situ micro-tensile testing during hydrogen charging with glass cell and (b) magnified view of (a)..... **35**
Figure 7.1 : Microstructures of (a) finely-grained SDSS, (b) coarsely-grained SDSS, (c) 10 hours pre-hydrogen charged coarsely-grained SDSS, and (d) 19 days pre-hydrogen charged coarsely-grained SDSS (repolished) and arrows indicate blisters formed in the ferrite phase. **37**
Figure 7.2 : Tensile test results of (a) the finely-grained SDSS tested with 62 hours and 9 days hydrogen charged before the test and (b) the coarsely-grained specimens. The tests began within half an hour after the electrochemical charging process terminated. **38**
Figure 7.3 : Optical micrographs show the microstructure of the finely-grained SDSS with different pre-hydrogen charging before and after plastic deformation until catastrophic failure. The hydrogen absorption resulted in discrete brittle cracks at and around the necked region. **39**

Figure 7.4 : Optical micrographs show the microstructure of the coarsely-grained SDSS with different pre-hydrogen charging before and after plastic deformation until catastrophic failure. The hydrogen absorption resulted in discrete brittle cracks at and around the necked region. **41**
Figure 7.5 : SEM montage micrograph shows the fracture surface of the finely-grained microstructure without hydrogen pre-charging after straining until catastrophic failure. **41**
Figure 7.6 : SEM fracture surface of the finely-grained microstructure with hydrogen pre-charging for 9 days after straining until catastrophic failure. **42**
Figure 7.7 : Microstructure images of the coarsely-grained SDSS after in-situ testing using an additively manufactured electrochemical cell: (a) shows the specimen's lower surface that was in contact with the solution and (b) shows the specimen's upper surface that was not in contact with the solution. The upper surface is polished down to 1 μm diamond slurry finish, but the lower surface is ground up to grade 500. ..... **43**
Figure 7.8 : Microstructure images (a) show hydrogen charged and uncharged regions on the repolished specimen after the fracture. (b) shows secondary cracks on ferrite, and (c) is a magnified view of (b). **43**
Figure 7.9 : Electrochemical hydrogen charging cells made of (a) PLA and (b) glass used for in-situ tensile straining while simultaneously hydrogen charging. (c) shows the effect of hydrogen absorption time on the mechanical properties of coarsely-grained SDSS. **44**
Figure 7.10 : DIC results of the finely-grained specimen without hydrogen showing microstrain evolution at a tensile load of (a) 200 MPa and (b) 600 MPa. **45**
Figure 7.11 : DIC results of finely-grained specimen hydrogen charged for 62 hours showing microstrain formation at a tensile load of (a) 200 MPa and (b) 600 MPa. **46**
Figure 7.12 : DIC results of the finely-grained microstructure hydrogen charged for 9 days showing microstrain evolution during tensile loading at (a) 200 MPa and (b) 600 MPa. **46**
Figure 7.13 : DIC results of the finely-grained microstructure hydrogen charged for 9 days showing microstrain evolution with a high resolution during tensile straining at a load of (a) 200 MPa and (b) 600 MPa. **47**
Figure 7.14 : DIC results of no hydrogen, 10 hours, 19 days, and 73 days hydrogen charged coarsely-grained specimen at (i) 300 MPa, (ii) 670 MPa, and (iii) 730 MPa. **47**
Figure 7.15 : DIC results of coarsely-grained microstructure hydrogen charged for 73 days showing microstrain evolution during tensile load at 753 MPa. The arrows indicate cracks. **48**
Figure 7.16 : DIC results of coarsely-grained microstructure strained during simultaneous hydrogen charging. Strain formation occurred homogeneously all over the microstructure. **49**
Figure 7.17 : Magnified view of yellow square region in Figure 7.16. (a) Strain mapping of microstructure with DIC and (b) microstructure of in-situ tested super duplex stainless steel before deformation. **49**

IN-SITU MECHANICAL TESTING AND DIGITAL IMAGE CORRELATION OF SUPER DUPLEX STAINLESS STEELS TO UNDERSTAND HYDROGEN EMBRITTLEMENT

SUMMARY

Super duplex stainless steel contains ferrite and austenite phases in its microstructure in equal amounts, providing superior mechanical and corrosion properties to most single-phase stainless steels. The microstructure has a continuous ferritic matrix with austenite islands embedded in the ferrite phase. Super duplex stainless steel is a workhorse material used in many industrial applications where the conditions are extreme in terms of corrosion and mechanical loading. Exposure to such extremes is often associated with the liberation of atomic hydrogen. The microstructure can readily absorb formed hydrogen. However, the presence of hydrogen in high-strength microstructures is detrimental; it causes a decrease in load-bearing capacity and ductility, a phenomenon called hydrogen embrittlement. There are failure reports of super duplex stainless steel used in subsea applications with cathodic protection against corrosion. However, analysis of these failed components has shown that only duplex microstructures with an austenite spacing larger than 50 μm fractured due to hydrogen. Critical components with finer microstructures show outstanding endurance, and no failure of such duplex stainless steel has been reported. It has remained unclear why finely-grain duplex microstructures show such an exceptional resistance to hydrogen-induced cracking and why duplex stainless steel with coarse microstructure shows high susceptibility to hydrogen embrittlement.

This thesis aims to understand the hydrogen embrittlement of super duplex stainless steel with a small (10 μm) and large (30 μm) austenite spacing microstructure. An in-situ mechanical testing method was developed to study the effect of hydrogen absorption and mechanical strain on the susceptibility to hydrogen embrittlement. The testing method comprises a miniature-sized tensile specimen mounted on a micro-tensile tester, an electrochemical cell for in-situ hydrogen charging, and an optical microscope with an extended focal depth. The sample was continuously slowly strained (0.005 mm/min = $4.17 \cdot 10^{-6}$ s^{-1}) while the microstructure was imaged until fracture. The specimens were either electrochemically pre-hydrogen charged for up to 72 days and then tested or tested with simultaneous hydrogen charging using self-made electrochemical cells. The results were stress-strain curves and thousands of micrographs which all provide information about the deformation characteristics of materials. Then, these images were processed with digital image correlation software and strain maps were generated to understand local strain behavior.

The results have shown that hydrogen absorption caused mechanical softening in the austenite phase, while hardening was observed in the ferrite phase. In addition, the finely-grained duplex microstructure, which has more resistance to hydrogen embrittlement, developed far fewer strain heterogeneities than the coarse one. The austenite grains in the coarse microstructure became more plastically than the austenitic grains in the finer microstructure. Likewise, the ferrite became less affected

due to hydrogen absorption in the fine microstructure due to more hydrogen trapping at grain boundaries. It became understood that the magnitude and number of strain heterogeneities are the main reason for hydrogen embrittlement. It also became understood that as long as the austenite phase has the capacity for hydrogen absorption and mechanical straining, the entire microstructure is protected against brittle fracture.

SÜPER DUPLEKS PASLANMA ÇELİKLERİN HİDROJEN GEVREKLİĞİNİ ANLAMAK İÇİN YERİNDE MEKANİK TESTİ VE DİJİTAL GÖRÜNTÜ KORELASYONU

ÖZET

Süper dupleks paslanmaz çeliği mikroyapısında hem ferrit hem de östenit fazını bulundurduğu için mekanik özellikeri ve korozyon direnci tek fazlı paslanmaz çeliklere göre daha üstündür. Ferrit fazı ana matrisi oluştururken sürekli bir yapıya sahiptir, östenit fazı ise adacıklar halinde bulunur ve süreksiz bir yapıya sahiptir. Süper dupleks paslanmaz çeliği sahip olduğu özelliklerden dolayı bir çok endüstriyel alanda kullanılır ve bu alanlardan bazılarında hidrojene maruz kalabilir. Hidrojen süper dupleks paslanmaz çeliğin yük taşıma kapasitesinin düşmesine ve sünekliğinin azalmasına neden olur. Bu olaya hidrojen gevrekliği denir ve 1875 yılında ilk olarak Johnson tarafından ortaya atılmıştır. O zamandan günümüze kadar birçok çalışma yapılmıştır. Literatürde kabul görmüş birkaç mekanizma olmasına karşılık asıl mekanizma henüz hala anlaşılamamıştır. Hidrojen gevrekliğine sebep olan neden ise yayınabilir atomik hidrojenlerdir. Numune içerisine giren hidrojen, yüksek gerilim konsantrasyonu bölgelerine yayınır ve burada gevrekliğe sebep olur. Bu nedenle hidrojen gevrekliği direncini arttırmak için hidrojen gişirini engelleyecek kaplamalar ya da yayınabilir hidrojeni mikroyapı içerisinde tutabilecek partiküller oluşturulabilir. Böylece hidrojen girişini engelleyerek ya da yayınabilir hidrojenin yayınmasını engelleyerek hidrojen gevrekliği direnci arttırılır.

Hidrojenin yayınma katsayısı, ferrit fazında daha yüksektir: dolayısıyla, ferrit fazında daha hızlı yayınır fakat östenit fazında çok daha yavaştır. Östenit fazındaki çözünürlüğü ise ferrite fazına göre çok daha yüksektir. Bu da ferritin hidrojen kırılganlığına hassaslığını arttırır.

Literatürde en yaygın iki mekanizma, hidrojenle güçlendirilmiş dekohezyon ve hidrojenle güçlendirilmiş yerelleştirilmiş plastisite mekanizmalarıdır. Dekohezyon mekanizması hidrojenin yüksek hidrostatik gerilim alanlarına yayınması ve burada genişleyen kafes içerisinde fazla hidrojen miktarına ulaşılmasından kaynaklanır. Hidrojen, atomlar arasındaki bağ kuvvetini azaltır ve klivaj düzlemler arasında ayrılma gerçekleşir. Böylece kırılganlık meydana gelir. Hidrojenle güçlendirilmiş yerelleştirilmiş plastisite mekanizmasında ise hidrojen yüksek hidrostatik gerilim alanlarına yayınır ve dislokasyon hareketliliğini arttırır. Böylece yerel bir bölgede ciddi miktarda deformasyon gerçekleşir ve malzeme plastik limitine ulaşıp kırılır.

Bu tez çalışmasında, süper dupleks paslanmaz çeliklerin hidrojen gevrekliğini anlamak için yerinde mekanik deneyler gerçekleştirilmiştir. Bir malzemenin hidrojen kırılganlığının mekanik açıdan incelemek için genellikle literatürde yavaş gerinme hız deneyi uygulanır. Böylece yayınabilir hidrojene, kritik bölgelere yayınması için zaman tanınmış olunur. Hidrojen içermeyen numune kopana kadar çekilir. Daha sonra, başka bir numune belli bir süre elektrokimyasal olarak katodik yüklenerek içine hidrojen girişi sağlanır. Hidrojen yükleme işlemi bittikten sonra numuneye çekme testi gerçekleştirilir.

Son olarak da gerilim-gerinme eğrileri ve kırılma morfojileri incelenir. Böylece hidrojen ve mikroyapı arasındaki etkileşimin nasıl bir kırılmaya neden olduğu incelenir.

Bu çalışmada, minyatür çekme numuneleri kullanılarak mikro çekme testi cihazıyla dijital optik mikroskop altında deney gerçekleştirilmiştir. Dijital optik mikroskop z ekseni boyunca hareket edip birçok görüntü elde eder ve bunları birleştirir. Böylece numunenin her yeri odakta kalır. Çekme testi sırasında yüzey pürüzlülüğü artar ve numune odaktan çıkabilir. Dijital optik mikroskobu sayesinde deney boyunca her yerin odakta olduğu görüntüler elde edilir. Daha sonra bu görüntüler dijital görüntü korelasyonu yazılımı ile işlenir. Dijital görüntü korelasyonu, elde edilen görüntüler arasında korelasyon fonksiyonuna göre bağıntıyı hesaplar. Böylece deforme olmamış görüntü ile deforme olmuş görüntü arasındaki değişimleri, piksel yer değiştirmelerine göre bulur ve birim şekil değişimini hesaplar. Böylece numunenin mikroyapısı boyunca birim şekil değişimi haritalanması yapılmıştır. Hidrojen etkisiyle hangi fazda nasıl bir değişim olduğu gözlemlenmiştir. Östenitte ciddi bir yumuşama gerçekleşirken ferritte sertleşme görülmüştür. Malzemenin tümünde ise, hidrojen yükleme süresi arttıkça malzemenin mukavemetinde artış sünekliğinde ise azalma gözlemlenmiştir. Çekme testi sonrası numunelerin yüzeyleri tekrardan hazırlanmıştır ve optik mikroskop ile çatlaklar incelenmiştir. Çatlakların ferrit fazında olduğu ve ilerlediği, östenit fazına geldiğinde ise durduğu gözlemlenmiştir. Fakat bazen çatlakların, ince taneli östenit fazında da ilerlediği görülmüştür. Farklı tane boyutuna sahip olan numuneler de test edilmiştir ve ince taneli mikroyapının hidrojen gevrekliğine karşı daha dirençli olduğu gözlemlenmiştir. Süper dupleks paslanmaz çelikte, östenit ve ferrit arasındaki tane sınırı, kristal yapıların farklı olmasından dolayı hidrojenlerin tutunabileceği tercih edilecek bölgelerden bir yerdir. Dolayısıyla tane boyutunun az olması daha fazla tane sınırın olmasına neden olacaktır. Böylece yayınabilir hidrojen miktarında da azalma olacaktır.

Hidrojen gevrekliğini test etmenin bir diğer yolu da çekme testi yaparken hidrojen yüklemektir. Böylece malzeme içerisine sürekli yayınabilir hidrojen bulundurulur ve bu düzeneğe yerinde çekme ve hidrojen yükleme deneyi denir. Bu deney gerçekleştirildiğinde ise hidrojenin etkisiyle malzemenin hem mukavemeti hem de sünekliği azalmıştır. Malzeme daha erken mukavemet seviyelerinde plastik deformasyona geçmiştir. Fakat mikroyapının izlenmesi bu deney düzeneğinde mümkün olmamıştır.

Tez çalışmasında özgünlük olarak yerinde elektrokimyasal hidrojen yükleme ve çekme testi hücresi tasarlanmıştır. Böylece numuneye hem çekme testi uygulanırken hem de numunenin alt yüzeyinden hidrojen yüklenmiştir ve eş zamanlı olarak da numunenin üst yüzeyinden mikroyapı gözlemlenmiştir. Bu sayede numunenin üst yüzeyinde herhangi bir kirlenme olmadan yüksek çözünürlükte görüntüleri elde edilmiştir. Daha sonra mikroyapı görüntüleri dijital görüntü korelasyonu ile işlenmiş ve deformasyon davranışı analiz edilmiştir. Diğer yapılan deneyde gözlemlenen östenit yumuşaması burda da gözlemlenmiştir. Fakat onun dışında hem ferrit hem de faz sınırlarında da ciddi bir yumuşama gerçekleşmiştir. Dolayısıyla yerinde deney gerçekleştirildiğinde yayınabilir hidrojen mikroyapının yumuşamasına ve erken seviyede plastik deformasyona geçmesine neden olmuştur. Bu da hidrojenin dislokasyon hareketliliğini arttırmasından dolayı kaynaklanır.

Mikroyapı içerisine giren hidrojen dislokasyon etrafın bir koruyucu atmosfer oluşturur ve dislokasyonla beraber hareket edebilir. Hareket ederken de etrafında sürekli olarak

konfigürasyonunu sağlayabilir. Bu sayede dislokasyonun diğer dislokasyonlarla ya da diğer yapı içerisindeki diğer hatalarla arasındaki etkileşimi azaltır. Bu sayede tane sınırında toplanmış dislokasyonlar arasındaki itici güç azalır ve birbirlerine yaklaşır. Bu da belli bir bölgede gerilim artışına ve aynı zamanda hidrojen miktarı artışına da neden olur. Böylece boşluk oluşumu ve daha sonra da çatlak oluşumuna neden olur. En sonunda ise kırılganlığa neden olur.

1. INTRODUCTION

Most of humanity's energy supply comes from fossil fuels such as oil, natural gas and coal. However, while fossil fuels ensure convenience in providing energy, they also cause severe damage to nature. Fossil fuels are both limited and unevenly distributed around the world. Moreover, it is predicted that the world's energy needs will increase by two times in 2050 [1].

The CO_2 gas released from fossil fuels threatens the world's climate. A large part of the CO_2 emission comes from metal, especially steel production. For this reason, studies are carried out on more innovative and cleaner steel production. Thus, hydrogen, abundant globally and a more sustainable opportunity, is an essential resource. However, hydrogen does not provide a political trump since it is found worldwide and leaves water instead of CO_2 in production [1–3].

While hydrogen is a good resource, it also has a drawback. In its atomic form, hydrogen can enter metals' microstructure during production or service conditions and cause brittleness, a phenomenon known as hydrogen embrittlement. Although hydrogen embrittlement is a subject that has been studied for over 140 years, its root cause is still not fully understood [4,5]. What has become clear is that the susceptibility to hydrogen embrittlement increases with the tensile strength of steels. Therefore, hydrogen embrittlement must become understood for safe and long-term applications in harsh environments.

Among all stainless steel families, super duplex stainless steels (SDSS) show exceptional resistance to hydrogen embrittlement and corrosion. The microstructure SDSS is composed of equal amounts of ferrite and austenite phases. As a result, they provide superior mechanical properties and corrosion resistance to most counterpart single-phase stainless steels. Therefore, SDSSs are preferred in harsh environments such as underwater pipelines and pressure vessels where both hydrogen and mechanical loads are found. However, their deformation behavior differs from other materials. The deformation characteristics in the presence of hydrogen are complex since introducing hydrogen into the material typically causes different effects in the

two phases [6,7]. Therefore, understanding the effect of hydrogen on the material properties of SDSS is very important for designing materials more resistant to hydrogen embrittlement.

2. MOTIVATION AND AIM OF RESEARCH

The research of this thesis aims to better understand the susceptibility to hydrogen embrittlement of grade 25Cr-7Ni SDSS with different microstructures, namely small (≈ 10 μm) and large (≈ 30 μm) austenite spacing. The further aim was to understand the effect of the hydrogen charging method, i.e. in-situ during mechanical straining and pre-hydrogen charging for up to 72 days, on the extent of hydrogen embrittlement. The research motivates to employ SDSSs longer and safer in harsh and critical environments.

3. SCOPE OF RESEARCH

This thesis studied the susceptibility to hydrogen embrittlement by characterizing the micro-mechanical deformation behaviour of grade 25-7Ni SDSS. First, micro-tensile specimens with a gauge length of 25 mm were subjected to electrochemical charging of atomic hydrogen for up to 72 days. Then, the samples were tested using a micro-tensile tester while continuously imaging the microstructure using a digital optical microscope. The micrographs were then processed using digital image correlation (DIC) software, and von Mises strain maps were generated. Finally, the deformation behaviour of microstructures with small and large austenite spacing was compared. Furthermore, in-situ tensile measurements with simultaneous microstructure imaging were conducted using a self-designed electrochemical cell during in-situ hydrogen charging. Finally, the effect of in-situ and ex-situ hydrogen charging on the micro-mechanical deformation characteristics was compared.

4. LITERATURE REVIEW

The first documentation of hydrogen embrittlement goes back to the 1875 publication by *Johnson*. It was reported that hydrogen caused a severe decrease in the toughness and brittleness of steel upon contact with an acid solution [8]. Later, this phenomenon was coined hydrogen embrittlement in the literature. Johnson performed a series of experiments to understand some fundamental aspects of hydrogen embrittlement. First, he immersed a steel wire in acid and later noticed that the material fractured more easily. Johnson repeated such experiments in different solutions. Finally, he noted that the brittleness was only caused by acids that release hydrogen ion due to the reaction of the material with the acid. Thus, the conclusion was that hydrogen, not acid, caused embrittlement. However, after removing the metal from the solution, the steel regained its initial toughness when the experiment was done with some delay. Hence, a further conclusion was that hydrogen embrittlement is reversible. Johnson performed further tensile experiments in a glass tube full of hydrogen gas and observed no embrittlement. Likewise, no embrittlement was observed when the experiments were done in water with continuous hydrogen purging. Hence, it became clear that only the diffusible hydrogen caused embrittlement. Later it has also become understood that the trapped hydrogen atoms are innocuous [4].

Johnson performed tensile experiments also in an alkaline solution and charged the steel electrochemically with hydrogen. The results were the same. Johnson conducted further research to understand the steel's tensile strength effect on high embrittlement. He noted that the susceptibility to hydrogen embrittlement increased with increasing tensile strength. In addition, Johnson noticed the outflow of hydrogen gas from the wetted fracture surfaces of the samples [4]. The latter observation has shown that most of the hydrogen leaves the microstructure upon the termination of the experiments. The microstructure absorbs hydrogen due to a driving force produced by corrosion reactions (with the acid) [8].

However, Johnson's experiments did not provide any information about the mechanism of hydrogen embrittlement. Over the past 140 years, a few models have been proposed for the embrittlement mechanism [5], but hydrogen embrittlement has

not become fully understood. However, it has become understood that a few parts-per-million (ppm) hydrogen ingress in the microstructure seriously affects the load-bearing capacity of metallic materials [5,9]. The mechanisms accepted in the literature are

I. hydrogen enhanced decohesion (HEDE),

II. hydrogen enhanced localized plasticity (HELP),

III. adsorption induced dislocation emission (AIDE),

IV. hydride formation and fracture, hydrogen enhanced strain induced vacancies (HESIV), and

V. the defactant concept.

It is also said that these mechanisms might cause embrittlement with a synergistic effect.

4.1 Hydrogen Embrittlement Mechanisms

4.1.1 Hydrogen-enhanced decohesion (HEDE)

HEDE is one of the most common mechanisms in the literature, reported first in 1926 by *Pfeil* [10]. The HEDE mechanism states that hydrogen reduces the lattice cohesion between cubic cleavage planes and grain boundaries. Later, *Troiano* extended the HEDE theory that the reason for the decohesion is that the electrons of hydrogen enter the 3d shell of the iron, causing an increase of repulsive forces between the atoms and tensile separation on the atomic scale was documented at early stress levels [11]. Later, *Oriani et al.* further improved the theory and stated that a threshold hydrogen concentration is needed to reduce the bond strength between atoms [12]. The accumulation of hydrogen on susceptible sites in the microstructure creates crack nuclei. Then, other hydrogen atoms are attracted, producing high hydrostatic stress fields in front of the crack tips. The lattice expands due to the positive hydrostatic tension fields, and the stress-induced diffusion of hydrogen occurs here, reducing the interatomic cohesion force. The result may often become an unexpected early fracture in the materials.

4.1.2 Hydrogen-enhanced localized plasticity (HELP)

HELP was first proposed by *Beachem* [13] and later developed by *Birnbaum, Sofronis and colleagues* [14–16]. Hydrogen is said to diffuse into high hydrostatic stress fields around the crack tip, facilitating dislocation movement resulting in extensive local plastic deformation (Figure 4.1). Hydrogen atoms form an atmosphere around the dislocation and move with the dislocation.

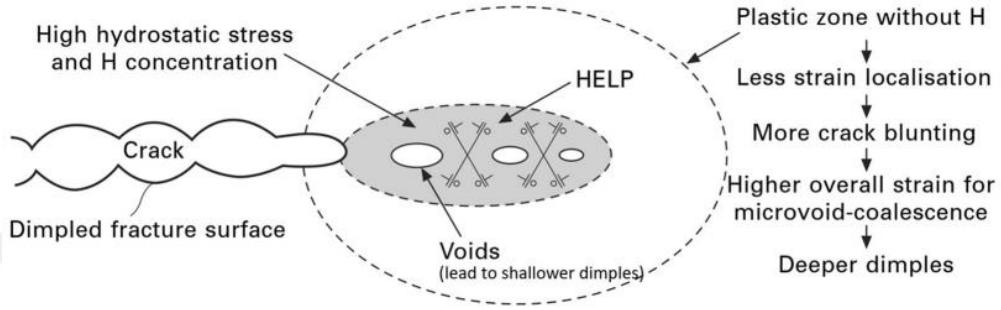

Figure 4.1 : Schematic representation of the HELP mechanism [5].

This hydrogen atmosphere reduces the repulsive interactions of the dislocation with other dislocations or particles, facilitating dislocation interactions and resulting in rapid dislocation multiplication due to reduced core energy and Peierls stress of dislocation activation. The repulsive forces between dislocations are reduced by absorption at the dislocations [15]. The increase in the dislocation activity due to the presence of hydrogen in the lattice was proven by in-situ transmission electron microscopy (TEM) experiments [16]. Significant local plasticity was observed at low stress and strain values, causing the material to exceed the plastic limit in local regions. Hence, a ductile type fracture occurred due to the formation and coalescence of micro-voids.

4.1.3 Adsorption-induced dislocation emission (AIDE)

The AIDE mechanism was proposed by *Lynch* [17]. It occurs due to hydrogen adsorption to the crack tip, facilitating dislocation nucleation and emission. Thus, dislocation emission is provided at lower stress values, and crack propagation is enhanced by dislocation emission. Hydrogen adsorption weakens atomic bonds within a few atomic distances and facilitates dislocation emission, favouring crack propagation at lower stress values and material fracture (Figure 4.2). The mechanism is based on the interaction of the surface and hydrogen.

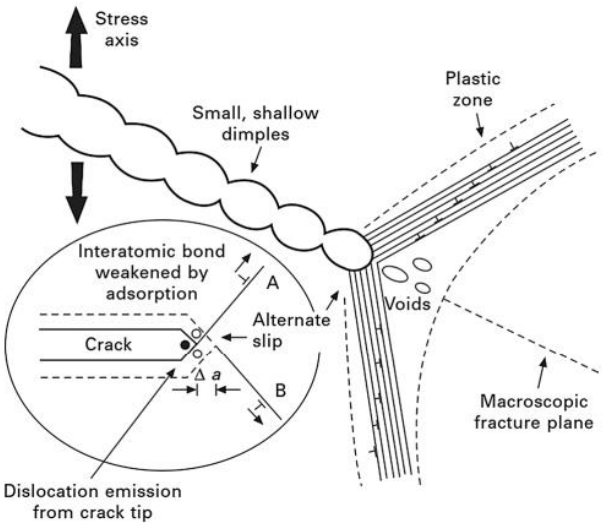

Figure 4.2 : Schematic representation of the AIDE mechanism [5].

4.1.4 Hydride formation

The mechanism of hydride formation and fracture was first proposed by *Westlake* [5]. However, hydrides are documented only in some materials, such as nickel- and titanium-based alloys. However, quasi hydrides were also reported in SDSS [18] — the absorption of hydrogen results in hydride formation leading to extensive stresses at the interphase [5,18]. Hence, cracks can initiate. Although hydrides have been reported to be brittle [5], they cannot undergo plastic deformation and fracture. Thus, the crack propagates through the brittle hydride phase and stops in the soft matrix. Then, the hydride phase is formed again at the progressive crack tip and fractures (Figure 4.3). Hydrogen accumulation, hydride formation and cracking occur reiteratedly until catastrophic failure.

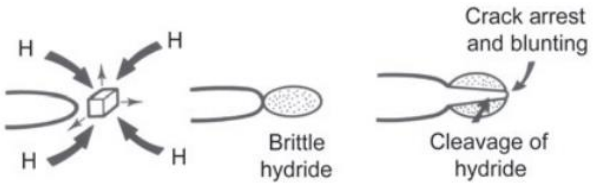

Figure 4.3 : Schematic representation of the hydride formation and fracture mechanism [5].

4.1.5 Hydrogen-enhanced strain-induced vacancies (HESIV)

The HESIV mechanism was proposed based on thermal desorption spectrometry (TDS) experiments, which showed that the hydrogen desorption rate decreased when below 200 °C. The mechanism refers to the annihilation of vacancies. Strain-induced vacancies increased with hydrogen ingress. The formation of vacancies is facilitated

due to hydrogen entry and nanovoid formation by combining vacancies. These nanovoids cause premature fracture near areas of high hydrostatic stresses [19,20].

4.1.6 The defactant concept

The defactant concept was introduced by Kirchheim in 2009. It is based on the thermodynamics of the interaction of hydrogen and defects within the material. The term defactant is a derivative from the surfactant theory. Surfactants (**Surf**ace **Act**ive **A**ge**nt**) are substances that lower the surface energy of liquids. Likewise, hydrogen atoms reduce the formation energies of defects. Therefore, hydrogen is a defactant (**Def**ect **Act**ive **A**ge**nt**). Kirchheim provided the following thermodynamic equation 4.1,

$$\Gamma_H \equiv \frac{1}{V}\frac{\partial n_H}{\partial \rho}\,|_{V,T,\mu_H,n_B} \tag{4.1}$$

where Γ, a positive value, describes the ratio of the amount of defactant atoms and the defect density, V is the volume, n_B is the number of solvent atoms, n_H is the number of hydrogen atoms, T is the temperature, and μ is the chemical potential.

The defactant concept explains why dislocations and vacancies can be formed easier due to absorbed hydrogen in the microstructure. Hydrogen atoms accelerate dislocations and facilitate Kink pair formation. Thus, the reason for hydrogen embrittlement is that hydrogen reduces the formation energies of defects (cracks) [21–23].

4.2 Super Duplex Stainless Steel

Super duplex stainless steel is highly-alloyed stainless steel with austenite and ferrite phases at approximately equal fractions in the microstructure. Duplex stainless steels are categorized according to their pitting resistance equivalent (PRE) values. SDSS are steel groups with PRE values of more than 40. Since it contains both austenite and ferrite in its structure, the strength of SDSS is higher than ordinary austenitic stainless steel and is more resistant to pitting corrosion. SDSS are also less expensive than austenitic stainless steels because they contain less nickel. Its toughness is higher than regular ferritic stainless steel and more resistant to hydrogen embrittlement. The microstructure has a continuous ferrite matrix in which austenite islands are

discontinuously embedded. During solidification, the first ferrite phase forms, and then the austenite phase forms. After several hot and cold rolling treatments, the duplex microstructure is formed between 1200 – 1000 °C. Therefore, the grains are typically elongated along the rolling direction but are not necessarily textured. Holding the microstructure at temperatures below 1000 °C, unwanted phases such as sigma, chi, nitrides or alpha prime and alpha double prime can occur. Therefore, exposure to temperatures between 300 – 1000 °C must be avoided [24].

4.3 Deformation of Metals

Mechanical properties describe the behavior of a material under stress and the response of the material to stress is deformation. When external tensile stress is applied to the material, the atoms first stretch and begin to displace after exceeding a specific limit. This limit is the yield strength. Before yield strength, the material exhibits elastic deformation behavior, indicating that the atoms will return to their original positions if the applied force before the yield strength is removed. After yield strength, the material exhibits plastic deformation behavior, and when the force is removed, the atoms cannot return to their former positions; hence, the resultant deformation is permanent. Hooke's law explains the deformation in the elastic region. The applied stress and the resulting strain are in a linear connection named the modulus of elasticity. The slope of the modulus of elasticity also depends on the bond strength of the atoms. The stronger the bond, the higher the slope. A higher modulus of elasticity indicates that elastic deformation will be difficult [25–27]. Equation 4.2 for the modulus of elasticity is given below.

$$E = \frac{\sigma}{e} \tag{4.2}$$

E is the modulus of elasticity, σ is the stress, and e is the strain [25–27].

The resistance of the material to the externally applied tension shows that its strength. This depends on the arrangement of the atoms in the material. Atoms are arranged in a particular periodic order in the material, called a crystal structure. In these crystals, some are arranged in different directions, some in the same direction, and the places where they coincide are called grain boundaries. The crystals growing in the same direction form a grain. Therefore, the material's mechanical properties differ according

to its atomic structures, crystal structures, grain sizes, grain directions and alloying elements [25–27].

Deformation occurs by different mechanisms. There are two basic mechanisms in a deformation that takes place; these are slip and twinning. Slip is the most common deformation mechanism, and deformation occurs primarily by slip. Mechanical twinning occurs at low temperatures and high strain rates, where a slip cannot happen. Twinning is a process that results in a mirror-like positioning of atoms according to twin boundaries [25–27].

The slip process is the sliding of atomic planes over each other. After the tensile test was performed on single crystal magnesium, it was observed that there were step marks on the surface when the surface was examined at high magnifications. When the crystallographic analysis of these steps was made, it was seen that they were the densest planes in the crystal structure. This type of deformation is called slip. Traces on the surface are also called slip lines or slip traces [25–27].

When plastically deforming a specimen, all atoms bonded in the plane must be broken and move an atomic distance for a slip to occur. The theoretical calculation is made for this, and the required strength is very high. However, when the sample is plastically deformed, slip is performed at much lower stress values. This is because crystals are not perfect and contain defects. One of these defects is the dislocations, which we call line defects. Dislocations are known as inserted extra half-planes into a perfect arrangement of atoms. This extra plane distorts the atomic arrangement around dislocation. During deformation, it is sufficient to break only a few bonds around the dislocation instead of breaking the bonds of all atoms in the plane. Thus, deformation can occur at much lower stress values [25–27].

Slip occurs in different planes and directions in materials with other crystal structures. The most minor symmetrical and repeated structures of crystal are called unit cells. The ferrite phase in duplex stainless steel has the body-centered cubic (bcc) crystal structure, while the austenite phase has the face-centered cubic (fcc) crystal structure. The bcc crystal structure is such that there will be 4 atoms in the corners and an atom in the center, as shown in Figure 4.5 [25–27].

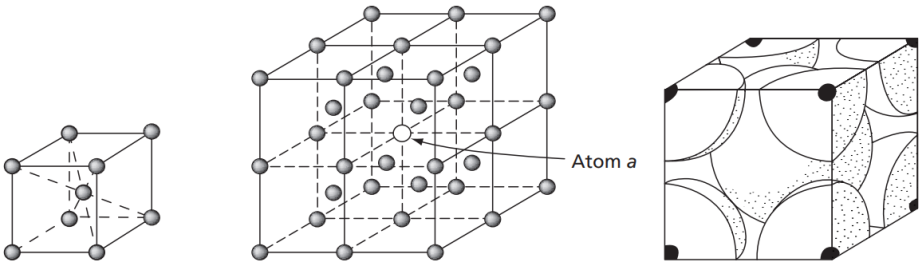

Figure 4.4 : Schematic representations of bcc unit cell [26].

Since the atoms in the corners are shared by 8 unit cells, the bcc crystal structure contains 2 atoms together with the atom in the center. The fcc crystal structure contains atoms at the corners and surface centers as seen in Figure 4.5. Atoms on surfaces are shared by 2 unit cells. While an atom comes from the corners, three atoms come from the surfaces, and it contains 4 atoms in total [25–27].

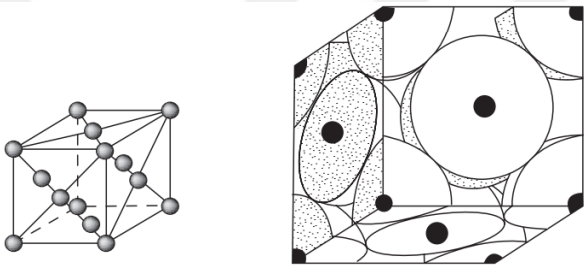

Figure 4.5 : Schematic representations of fcc unit cell [26].

The atoms in the bcc crystal structure touch each other along the diagonal and form the densest direction. There are 8 atoms closest to the central atom, and the coordination number of the bcc structure is 8. In the fcc crystal structure, the atoms on the diagonal surface touch each other and form the densest direction. The coordination number of the fcc crystal structure is 12. The atomic packing factor (APF) of fcc crystal structures is 0.74, while bcc's is 0.68. Equation 4.3 for APF is given below [25–27].

$$APF = \frac{volume\ of\ atoms\ in\ a\ unit\ cell}{total\ unit\ cell\ volume} \tag{4.3}$$

The planes in which the dislocations move are called slip planes and the direction is called the slip direction. The slip plane and the slip direction form the slip systems. The slip plane and slip direction also occur in the densest planes and directions. Table 4.1 below gives the densest directions and planes for fcc and bcc [25–27].

Table 4.1 : Slip plane, direction and number of slip systems of crystal structures [25].

Crystal Structure	Slip Plane	Slip Direction	Number of Slip Systems
fcc	{111}	<110>	12
bcc	{110}, {211}, {321}	<111>	48

The fcc structure has 12 slip systems in total. The bcc structure has more, but not all are active at room temperature. Materials fcc structure are softer and can be easier deformed than bcc materials because fcc has a closed-packed system. The distortion created by the dislocation in the fcc structure spreads over a wider area, so the dislocation width is wider. The bcc structure has thinner dislocation width. The Peierls stress is the lowest stress required to move a dislocation. It is also known as the internal resistance of the lattice. Peierls stress can be calculated with the equation 4.4,

$$\tau = Ge^{\frac{-2\pi w}{b}} \tag{4.4}$$

τ is the Peierls stress, and w is the dislocation width. Therefore, it is easier to initiate dislocation motion in fcc structures. Larger dislocation width leads to lower Peierls stress [25–27].

4.4 State-of-the-art Testing for Hydrogen Embrittlement

The characterization of hydrogen embrittlement is done by (i) detecting hydrogen in the microstructure and by (ii) mechanical testing. Detecting hydrogen in microstructures is challenging and often done by neutron radiography, TDS, atom probe tomography (APT), silver reduction and decoration, secondary ion mass spectrometry (SIMS), and the scanning Kelvin probe methods [28]. However, it is beyond current science to detect hydrogen in-situ and in real-time during mechanical testing. Therefore, the work in this thesis concentrates on in-situ testing for hydrogen embrittlement.

There are thousands of publications about mechanical testing of hydrogen-absorbed high-strength steels and stainless steels. While a summary of key results obtained from classic mechanical testing will be given, this thesis focuses only on research conducted on in-situ mechanical characterizations. Traditional mechanical testing is performing tensile tests on pre-hydrogen specimens and comparing them with non-hydrogen specimens, followed by examining the stress-strain curves and the fracture

morphologies. The tests are done under (i) static or (ii) dynamic load. Testing under static loading, also known as constant load testing, is done to tell if a material under elastic strain fails due to the presence of absorbed hydrogen. The material is subjected to a static mechanical load while infusing hydrogen into the microstructure. As a result, one can obtain the threshold hydrogen concentration for crack formation [29].

Chai et al. [30] investigated the hydrogen embrittlement of duplex stainless steels (SAF 2057 and SAF 2906) by an in-situ constant load test. When they examined the samples after the experiment, it was seen that voids were formed at the ferrite grain boundaries and austenite-ferrite grain boundaries, and then voids turned into microcracks. It has been said that this causes ferrite cleavage fractures. In austenite, on the other hand, it was stated that a stress concentration region was formed due to dislocation mobility and pile-up formation, which again caused a ferrite cleavage fracture. Crack propagation is discontinuous. It was observed that while cracks propagated along the ferrite, they stopped at the austenite and moved along the ferrite.

Dynamic testing, also known as slow strain rate testing (SSRT), performs tensile testing at strain rates typically between 10^{-6} – 10^{-2} s^{-1} during continuous hydrogen charging, often by electrochemical means [29]. The reason for slow straining is to give hydrogen enough time to interact with the microstructure. A microstructure is susceptible to mechanical degradation due to hydrogen if its presence results in loss of elongation or toughness.

Oltra et al. [31] studied the embrittlement of the austenite phase in duplex stainless steel in a hydrogen environment. They applied a slow strain tensile test in a hydrogen gas environment (in-situ). The experiments were stopped before the specimen fractured and the cracks were examined. When the results were examined, it was seen that there were zig-zag shape cracks. When SIMS analysis was performed, deuterium was observed around the cracks in austenite. They explained these cracks as follows; the ferrite phase was fractured brittle and across to the austenite-ferrite grain boundary so that hydrogen atoms came to the austenite phase from the ferrite phase. Later, it was said that these hydrogen atoms increase the deformation locally, and the dislocations pile up at an obstacle. Then, microcrack formed at pile-up when a sufficient amount of dislocation was reached. Then, the crack progressed from the first crack and formed a zig-zag crack. Finally, it was observed that the crack stopped when the hydrogen

atmosphere was removed from the chamber. However, the specimens were post-mortem examined after the test was stopped, and a conclusion was made accordingly.

The mentioned testing methods provide only limited information. Therefore, more advanced in-situ experiments have been tried to be designed. Hence, it is aimed to understand the hydrogen microstructure interaction during hydrogen absorption while the material is strained. Furthermore, another characterization method was added to the in-situ setup (under tension and hydrogen charging, or a different couple of situations), and it was desired to learn what happened at the time of the event.

Örnek et al. designed an experimental setup that characterizes the microstructure of SDSS during cathodic hydrogen charging under constant load. At the same time, local diffraction patterns with high energy x-ray diffraction with a spatial resolution of 20 microns were measured (Figure 4.6) [32].

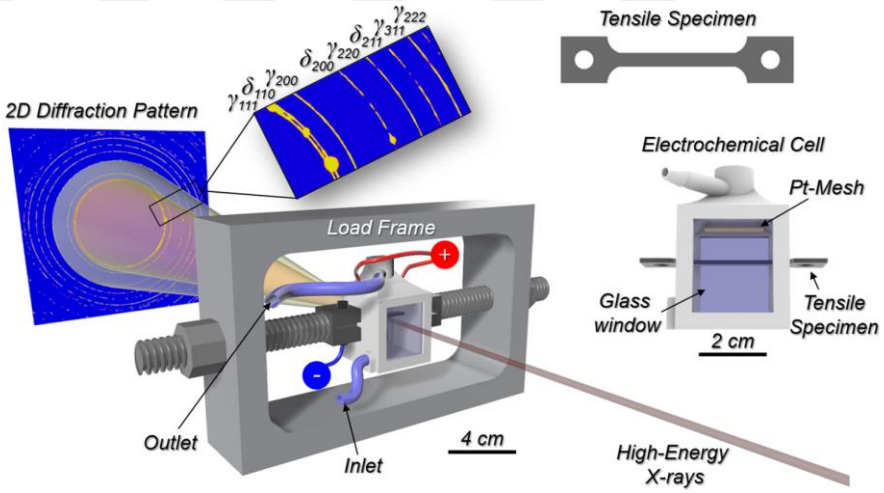

Figure 4.6 : Schematic representation of in-situ experimental setup [32].

The research outcome was that hydrogen changes the deformation characteristics of SDSS by producing intense local strain formation sites that develop primarily in the austenite phase. Hydrogen caused the evolution of tensile strains perpendicular to the surface, indicating the path of possible crack formation. An increase in the amount of strain was observed as the hydrogen charging time increased [32].

Another in-situ setup was performed by *Ferreira et al.* [16] in an environmental TEM. Hydrogen gas was introduced into the TEM cell, upon which the hydrogen dissociated due to the electron beam energy. As a result, atomic hydrogen is infused into the microstructure. The dislocations piled up at the grain boundary with the hydrogen

ingress. The dislocation density increased with increasing hydrogen absorption supporting the HELP theory [16].

Kim and Tasan [33] designed another in-situ setup. In an electron microscope, a self-designed electrochemical cell was used to charge a titanium alloy with hydrogen from the bottom of the specimen while imaging the microstructure of the top surface (see Figure 4.7).

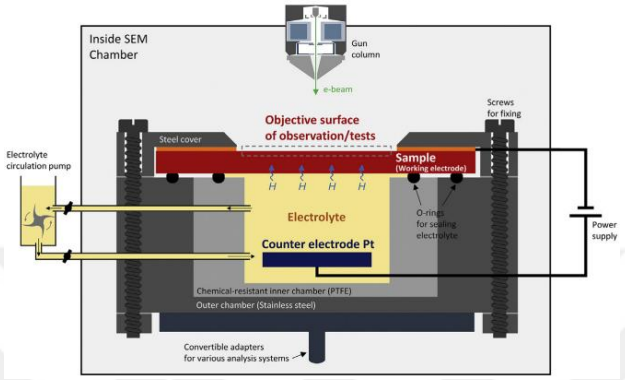

Figure 4.7 : Schematic representation of an in-situ experimental setup for hydrogen charging [33].

Hydride evolution was monitored, and it could be shown that the hydride develops at grain boundaries. A specimen made of duplex stainless steel was also tested. It could be shown that there is more effusing hydrogen from the ferrite phase by an electrochemical decoration of silver. Effusing hydrogen reduces silver ions to metallic, which are bright spots in secondary electron imaging. However, the experiment was conducted ex-situ, and no strain was applied. Hence, the mechanical deformation of duplex stainless steel was not characterized. Furthermore, the cell was used for nanoindentation on ferritic stainless steel. It was observed that the material hardened with the absorbing hydrogen. Hence, hydrogen hardens the ferrite phase.

Koyama and his colleagues pre-charged duplex stainless steel with hydrogen and then observed its surface in a scanning electron microscope (SEM) with the electron channelling contrast imaging (ECCI) method (see Figure 4.8). No external force or tensile test was applied to the sample. Since hydrogen diffusion in FCC materials is much slower, the hydrogens diffusing out can be neglected during the experimental setup. Hydrogen is released from the sample in the vacuum, and it has been observed that hydrogen facilitates the dislocation movement. They explained that the driving force that increases the dislocation mobility is due to the high-stress concentration caused by the hydrogen accumulation at the grain boundaries [34].

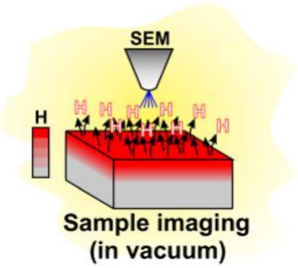

Figure 4.8 : Schematic experimental setup to investigate hydrogen desorption effects on dislocation mobility [34].

However, understanding the local deformation behavior of microstructures with hydrogen is essential to detecting the most susceptible sites. The main disadvantage of only testing is that hydrogen-microstructure-strain interactions do not become entirely understood. In this thesis, the SSRT technique was employed with an in-situ approach. The idea is to measure mechanical properties with simultaneous microstructure imaging to understand local deformation characteristics. Unique insights into the mechanical behavior of microstructure will be obtained by in-situ mechanical testing. Thus, interaction of the different phases in SDSS with hydrogen will be observed how behaves at the micro level.

4.5 Hydrogen Absorption

Different methods can be used to introduce hydrogen into the material. Among these, the most common ones are the absorption from the gas phase or the aqueous electrolytic state. In the gas phase, molecular hydrogen is adsorbed on the surface (physisorption), where it dissociates into atomic hydrogen. Then, atomic hydrogen infuses into the microstructure and diffuses into high-stress zones in the bulk material (Figure 4.9).

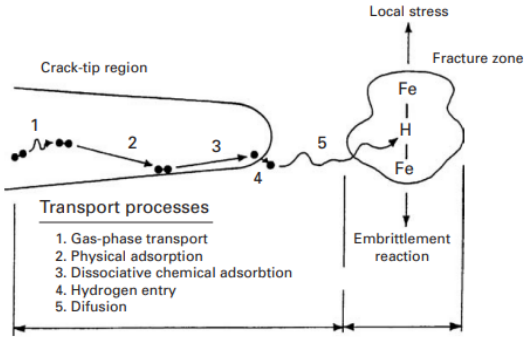

Figure 4.9 : Schematic illustration shows the gas-phase hydrogen absorption process into the bulk material and the resulting embryonic stage of the HEDE mechanism of hydrogen embrittlement [35].

Hydrogen absorption from an aqueous solution is also known as electrochemical hydrogen absorption. The magnitude of hydrogen ingress varies with the solution pH. Therefore, more hydrogen is produced at lower pH. In acidic solutions, hydrogen uptake is provided by reducing the hydrogen ions (proton) to atomic hydrogen that is first adsorbed and then becomes absorbed. In contrast, in alkaline or neutral pH, hydrogen entry is provided by the decomposition of water [36]. The equation 4.5 and equation 4.6 of the reactions are given below:

$$H^{+}_{(aq)} + e^{-}_{(M)} = H \quad (acidic) \tag{4.5}$$

$$H_2O + e^{-}_{(M)} = H + OH^{-}_{(aq)} \quad (alkaline\ or\ neutral) \tag{4.6}$$

The efficiency of electrochemical hydrogen absorption is on the order of 1-2%. This is because most hydrogen atoms recombine and leave the surface as gaseous molecular hydrogen [36]. The absorption efficiency can be increased by using a recombination poison which can increase hydrogen uptake by approximately 10-20%. Electrochemical hydrogen charging is a simple way of absorption compared to gaseous hydrogen [37].

4.6 Hydrogen Diffusion

After hydrogen has entered the material, it occupies lattice sites and moves by vacancies. Hydrogen prefers tetrahedral sites in the bcc crystal structure (ferrite) since tetrahedral sites are almost twice as large as octahedral sites. In the fcc crystal structure (austenite), hydrogen prefers octahedral sites. The diffusion coefficient of hydrogen in the ferrite phase is higher [38] than in the austenite phase because the distance between the closest tetrahedral sites in the ferritic structure is minimal. The distance between the nearest octahedral sites in the austenite is approximately two times longer. Therefore, the activation energy required for hydrogen diffusion in the ferrite is less [36,37]. However, austenite's hydrogen solubility is higher than that of ferrite.

Traps can inhibit hydrogen diffusion between interstitial sites of lattice in the microstructure. Potential wells of trap sites in the microstructure are deeper than interstitial sites. Hydrogen occupies trap sites and does not diffuse out. When hydrogen cannot diffuse out, these regions are called irreversible trap sites, and their potential is profound. The regions where hydrogen diffusion can reoccur are called reversible trap

sites, and it is easier for hydrogen to effuse. In the microstructure, trap sites for hydrogen are dislocations, grain boundaries, phase boundaries, solutes, inclusions, interface, precipitates, and vacancies [37].

Chen and colleagues observed the accumulation of hydrogen in microstructural defects with cryo-atom probe tomography. They showed that hydrogen is trapped at the interface between matrix and carbide, which is incoherent, at the dislocation core and grain boundaries [39]. Furthermore, the same experimental setup is also conducted on coherent small vanadium carbides, suggesting that hydrogen is seen in the bulk of carbides [40].

Mente and Boellinghaus [41] measured the diffusion coefficients in duplex stainless steel. The diffusion coefficient of the ferrite phase was reported as 1.5×10^{-5} mm^2/s, the austenite phase was 1.4×10^{-10}, the interface was 1×10^{-3}, and the interface contained a trap site was 1×10^{-15}. Turnbull showed that the duplex microstructure contributes to lower diffusion permeation because the hydrogen atoms have to move around the austenite grains during rapid diffusion in the ferrite phase [42]. The reported phenomenon has been called tortuosity.

5. CHARACTERIZATION TECHNIQUES/TOOLS USED

In this section, the characterization techniques used are described.

5.1 Metallography

Metallography is the science that describes the microstructure of materials. Tensile specimens were fabricated by cutting from the bulk material with an electrical discharge machine. After cutting, the samples were mechanically wet-ground using abrasive SiC sandpapers. Then, the specimens were polished using diamond paste slurries. Then, all samples were cleaned with ethanol, acetone and ultra-pure distilled water. Finally, the specimens were electrochemically etched in 10 wt.-% oxalic acid at 5 V, followed by etching in 40 wt.-% potassium hydroxide solution at 5 V for 3 seconds (all at room temperature). Thus, a contrast between the ferrite and austenite grains was obtained.

5.2 Micro-Mechanical Testing (DEBEN)

The tester is a miniature-sized device that enables in-situ tensile tests under the HIROX digital microscope (see Figure 5.1 and Figure 6.1). The tester has a travel length of 15 mm, giving 60 % strain. The specimens were mechanically elongated with a motor speed of 0.005 mm/min. The device was capable of applying a force of 5 kN.

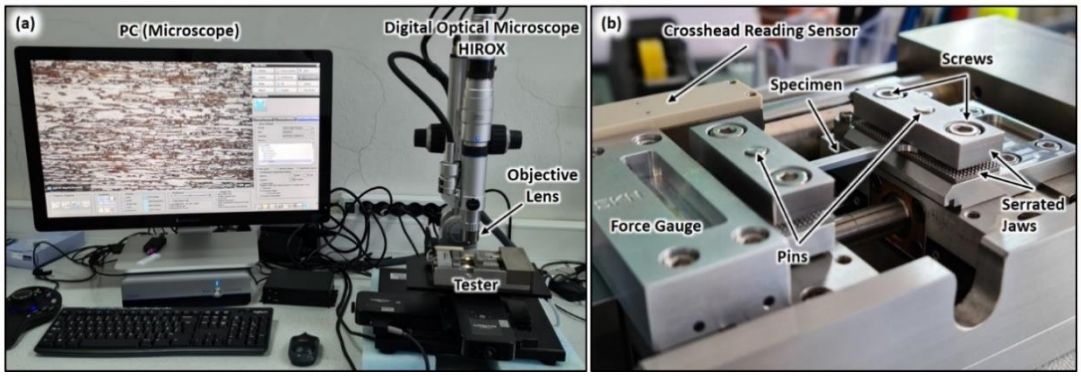

Figure 5.1 : Images of the (a) in-situ tensile test experiment with digital optical microscope and tester and (b) magnified view of the miniature-sized DEBEN tester.

During the tensile test, the tester collects elongation and force data with two data points per second. Then, the elongation and force values are converted into strain and stress using the tested specimen's geometric information. The stress-strain curves provide information about the mechanical properties such as elastic deformation, Young's modulus, plastic deformation, ductility, yield strength, tensile strength, and toughness.

5.3 Digital Optical Microscope (HIROX)

The HIROX microscope is assembled in a single column called an all-in-one focus lens system. Thus, there is no need to adjust focus when switching to another magnification. Another speciality of this microscope is that it has a large depth of field, which is needed for in-situ tensile testing (see Figure 5.1). In addition, the microscope has a motorized X-Y-Z stage and the option to stack images taken from several heights, producing micrographs with all regions in focus. Therefore, the microscope is well suited for continuously recording the microstructure when performing the tensile test. Some detailed information about magnifications, focal depth, the field of view, and the resolution is provided in Table 6.2.

5.4 Digital Image Correlation

DIC calculates changes in images taken from the same place in time-lapse [43]. The idea is to image the microstructure of a specimen during mechanical elongation. DIC recognizes changes in the microstructure that is invisible to the eye. Micro-deformation can be computed and quantitatively shown in strain maps.

The principle of DIC is explained in Figure 5.2. An array of pixels represents a figure. DIC subdivides an image into a user-defined subset that contains pixels in x and y directions. Figure 5.2 shows an undeformed subset that changed position and shape due to deformation. The undeformed subset has 6x6 pixels. DIC finds the correlation between the undeformed subset and the deformed subset, then calculates which pixel goes where. Thus, as a result of deformation, how much the subset has been displaced and how its shape has changed can be calculated. While performing the pixel tracking, it monitors the pixel in the center of the subset (P in Figure 5.2) and the surrounding pixels (Q in Figure 5.2) together since it is difficult to distinguish where a single pixel goes. Because there may be another similar pixel and it may represent an incorrect

result. Therefore, pixel tracking is performed as the center pixel and the surrounding pixels. The center pixel and the surrounding pixels form a subset. Therefore, the DIC tracks the subsets in the deformed and undeformed images and calculates the deformation based on how much it is displaced. The size of subset can be changed or deformed. It can be extended in one axis and shortened in another. Therefore, a square called a separate search field is defined to monitor the subset. This square starts from the top left of the sample and goes to the bottom right and scans. Furthermore, it searches for the subset that will give the closest result to the pixel group in the undeformed subset according to the correlation mathematical formula. After finding the displacement, it shows the strain mapping of the specimen by calculating its partial derivative [43–46].

The following mathematical equation 5.1 and equation 5.2 describes the relationship between undeformed and deformed subsets, from which the strain is calculated as shown in Figure 5.2.

$$x^* = x + u_x + \frac{\partial u_x}{\partial x}\Delta x + \frac{\partial u_x}{\partial y}\Delta y \tag{5.1}$$

$$y^* = y + u_y + \frac{\partial u_y}{\partial x}\Delta x + \frac{\partial u_y}{\partial y}\Delta y \tag{5.2}$$

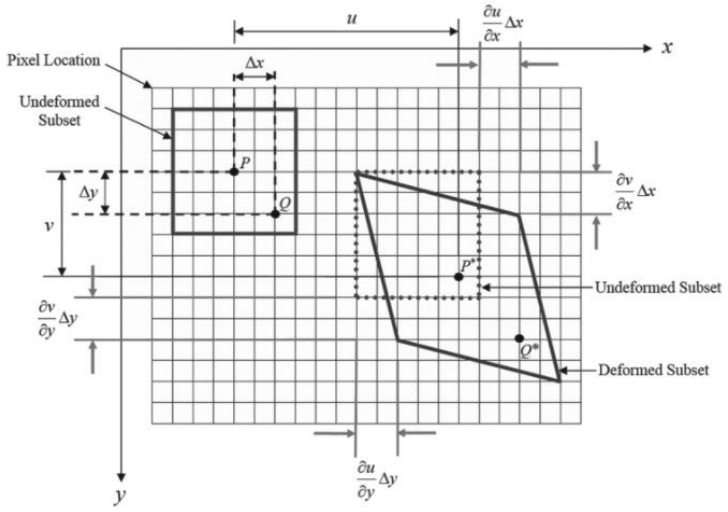

Figure 5.2 : Computation of displacement of deformed subset via DIC [45].

The coordinates of the points P and Q of the undeformed subset are in reference to an x-y coordinate system. The x* and y* show the position of the new subset after the deformation. u_x shows how much the P point is shifted along the x-axis due to the

deformation. u_y, on the other hand, shows how much the P point is shifted along the y-axis as a result of deformation. Δx and Δy represent the x and y-axes of the Q point selected at a certain distance from the P point. Therefore, by determining a secondary pixel (Q) in the subset, the displacement of other pixels will be calculated by finding how much its distance relative to the reference pixel in the middle changes as a result of deformation. $\frac{\partial u_x}{\partial x}$, $\frac{\partial u_y}{\partial y}$ $\frac{\partial u_y}{\partial x}$, and $\frac{\partial u_x}{\partial y}$ are the displacement gradients. Partial derivatives are taken to find out how much it changes in unit displacement. The derivative is the smallest change of an expression. To find how much u_x changes by a unit amount along the x-axis, partial derivative with respect to x is applied. Thus, the varying length of the subset along the x-axis is found. The same operation is done on the y-axis. Calculating how much u_x has changed along the y-axis is how much the slope has changed. Thus, normal (red expression in equations) and shear (blue expression in equations) strains are calculated [45]. Displacement gradients are differentiated to calculate the strains in directions as regards E_{xx}, E_{yy}, E_{xy} as shown in equations.

$$E_{xx} = \frac{1}{2}\left[\,2\frac{\partial u_x}{\partial x} + \left(\frac{\partial u_x}{\partial x}\right)^2 + \left(\frac{\partial u_y}{\partial x}\right)^2\right] \tag{5.3}$$

$$E_{yy} = \frac{1}{2}\left[\,2\frac{\partial u_y}{\partial y} + \left(\frac{\partial u_x}{\partial y}\right)^2 + \left(\frac{\partial u_y}{\partial y}\right)^2\right] \tag{5.4}$$

$$E_{xy} = \frac{1}{2}\left[\frac{\partial u_x}{\partial y} + \frac{\partial u_y}{\partial x} + \frac{\partial u_x}{\partial x}\frac{\partial u_x}{\partial y} + \frac{\partial u_y}{\partial x}\frac{\partial u_y}{\partial y}\right] \tag{5.5}$$

With the algorithms developed in the literature, second partial derivatives and DIC calculations have now started to progress enough to calculate point changes [46].

Before starting the DIC process, lower and upper limit values are entered for u_x, u_y, $\frac{\partial u_x}{\partial x}$, $\frac{\partial u_x}{\partial y}$, $\frac{\partial u_y}{\partial x}$, and $\frac{\partial u_y}{\partial y}$ values, and DIC quickly scans between these values to find the best correaliton value. The threshold for the correlation value should be at most 0.5 [43].

The results obtained while calculating strain with DIC contain some errors. This error may be caused by the microstructure of the material and the selected subset size. For the DIC to calculate with less error, the pixels and patterns in the subset must be distinguishable from each other. If a small subset is taken in a large grain and this grain does not have a distinctive pattern which is completely the same everywhere, it is

difficult to distinguish the deformed pixels and DIC cannot see these strains. Therefore, it is crucial to set the pattern and subset size. The smaller the subset size, the higher the resolution, but it becomes harder to distinguish pixels. Therefore, an optimum value should be chosen [44]. There are studies in the literature to calculate the deformation in the microstructure with higher resolution and less error [47].

Apart from this, different factors may cause errors during strain calculation. These may be caused by the experimental setup. For example, illumination-induced errors may occur in the microstructure observed with an optical microscope. Also, as the sample deforms, the pattern may become lighter. But there are algorithms to prevent them. In the experimental setup used in this research, the imaging of the microstructure was made with a digital optic microscope HIROX. As will be discussed in detail in the experimental section, micrographs are taken where the whole microstructure is focused, thanks to the digital microscope. But it takes 10 seconds to get 1 micrograph, and the tensile test continues during this time. Therefore, an error occurs. However, as a result of the calculation, the material's elongation amount is not greater than one pixel during the time a micrograph is taken. Furthermore, errors such as background noise that occurs during DIC are eliminated by filtering. When strains below 2% (at most) are filtered, background noise is prevented, and deformation can be calculated [48].

6. EXPERIMENTAL PROCEDURE

6.1 Material Investigated

Finely-grained (tube material) and coarsely-grained (bar material) commercial SDSS grades made of SAF 2507 (UNS S32750), obtained from Sandvik Technology, were tested. The chemical composition of the materials is provided in Table 6.1. The tube material had a wall thickness of 1.5 mm, and the bar material was a large block with a diameter of 297 mm. Several tensile specimens with a gauge length of 25 mm, a gauge width of 3 mm and a thickness of 1-1.5 mm were machined from the raw materials using electric discharge machining (EDM). The oxide scale from the EDM process was removed by grinding all sides of the specimens. One side of the samples was successively wet-ground from 400, 800, 1200, 2500 to 4000 grit SiC sandpapers. Then, the specimens were mechanically polished with 3 μm and 1 μm diamond slurries. After the polishing, the samples were electrochemically etched with 10 wt.-% oxalic acid (analytical grade from MERCK) by applying 2.5 V to the specimen for 10 seconds. The etching revealed the grain boundaries of both the austenite and ferrite phases. Then, further electrolytic etching was carried out with 40 wt.-% KOH (analytical grade from MERCK) solution for 1 second at 5 V to stain the ferrite phase to obtain phase contrast. Both etching treatments served as a pattern which is necessary for DIC computation.

Table 6.1 : Chemical composition (in weight percent) of the investigated SDSSs.

Material	C	Si	Mn	P	S	Cr	Ni	Mo	N	Fe
Tube	0.017	0.6	0.77	0.022	0.001	24.9	6.9	3.87	0.3	Balance
Bar	0.0016	0.25	0.8	0.019	0.0002	24.6	6.8	3.66	0.3	Balance

6.2 Microstructure Characterization

The HIROX RH-2000 digital optical microscope characterised the microstructure using several magnification lenses (Table 6.2). The microstructure of the etched specimens was imaged, and several montage images were made by 3D tiling to achieve

micrographs with all regions in focus. By doing so, a far larger field of view than those listed in Table 6.2 was achieved, contributing to improved statistical results.

Table 6.2 : Field of view and resolution information of the images taken with the HIROX digital microscope.

Magnification	Field of View	Working Distance	Resolution
140x	2462 μm	30.5 mm	1.28 μm
200x	1795 μm	30.5 mm	0.93 μm
400x	888 μm	30.5 mm	0.46 μm
500x	711 μm	30.5 mm	0.37 μm
600x	598 μm	30.5 mm	0.31 μm
800x	458 μm	30.5 mm	0.24 μm
1000x	359 μm	30.5 mm	0.19 μm
1400x	256 μm	30.5 mm	0.13 μm

The rolling direction of the materials characterized the microstructure. ImageJ software determined the phase fraction and austenite spacing from image analysis. 140x – 1400x magnifications were used. Several bright field images were taken from different regions of the specimens and saved in BMP format.

6.3 Electrochemical Hydrogen Charging

The electrochemical hydrogen charging was done to infuse hydrogen into the tensile specimens to understand the susceptibility to hydrogen embrittlement. First, tensile specimens were charged for up to 72 days to achieve varying hydrogen concentrations in the microstructure. The detailed charging protocol is listed in Table 6.3. Then, at room temperature, the electrochemical charging was done in a beaker of 200 mL solution of 0.01 M NaCl. Outside of the specimens' the gauge area was masked using epoxy and dried for 24 hours in ambient air to limit hydrogen uptake into the gauge area during the charging process. Then, the tensile samples were immersed in the solution and connected to a power supply's negative pole (cathode). Next, a platinum mesh was attached to the positive pole (anode) and immersed in the solution. The charging was done under galvanostatic control by applying a cathodic current (to the specimen) of 38 mA/cm². This current was chosen based on previous research [18,32,49]. After long-term hydrogen charging (for days), a film formed on the specimens' surface. These were later analyzed as platinum that dissolved and deposited onto the specimen during the polarization. The film has been removed by slight re-grinding using 4000 grit sandpaper, then repolishing and electrolytic etching

as explained above. This process removed a maximum of 5 μm. More than 30 specimens were tested.

6.4 In-situ Micro-tensile Testing of Pre-Hydrogen Charged Specimens

In-situ tensile testing consisted of mechanical elongation experiments of pre-hydrogen charged micro-tensile specimens with simultaneous microstructure imaging during continuous deformation. The specimen was mounted on the tester device using serrated jaws, pins and screws, and then a tension force of 5 N was applied to ensure firm mechanical contact between the pins and the specimen (Figure 6.1). Then, the serrated jaws were tightened, and the force reading was nulled. Then, the tensile test started. A tensile load was continuously applied under displacement control with a motor speed (extension rate) of 0.005 mm/min, corresponding to an engineering strain rate of $3.33 \times 10^{-6}\, s^{-1}$ until catastrophic failure. This motor speed was chosen because of two reasons: (i) the interaction of hydrogen with the microstructure is slow and highest in the strain range of 10^{-4} – $10^{-7,}$ and (ii) typically, 3-10 seconds were needed to acquire an all-in-focus image with the HIROX microscope. Since the testing was done slowly, 10 seconds, imaging did not cause a major error. During 10 seconds of imaging, the sample elongates by 0.83 μm, less than 1 pixel in size in a microstructure viewed with a 200x lens (Table 6.2). The tensile test began from half an hour to two hours (see Table 6.3).

Table 6.3 : Experimental conditions of in-situ micro-tensile testing of hydrogen pre-charged specimens.

Material	H-Charging	Test Started	Magnification	Time to Fracture
Tube	-	-	200x	28:05:46
Tube	62 hours	2.5 hours after charging	200x	27:27:51
Tube	9 days	30 min after charging	200x	17:50:31
Bar	-	-	200x	27:17:00
Bar	10 hours	30 min after charging	200x	14:04:22
Bar	19 days 20 hours	1 hour after charging	200x	7:24:04
Bar	73 days 2 hours	2 hours after charging	200x	7:25:32

Upon termination of the electrochemical polarization, hydrogen effusion takes place. However, due to the slow diffusion kinetics, especially in the austenite phase, the effusion time is far longer (days to weeks) than the tensile testing (typically 2-14 hours). The force was read with an accuracy of ± 1 N. The tester has no extensometer but only a crosshead reading sensor. However, DIC was used as a virtual extensometer (to be explained later). The tester's displacement read-out (crosshead information) was used for estimating the tensile strain. On the other hand, DIC served as a supplement for more accurate results.

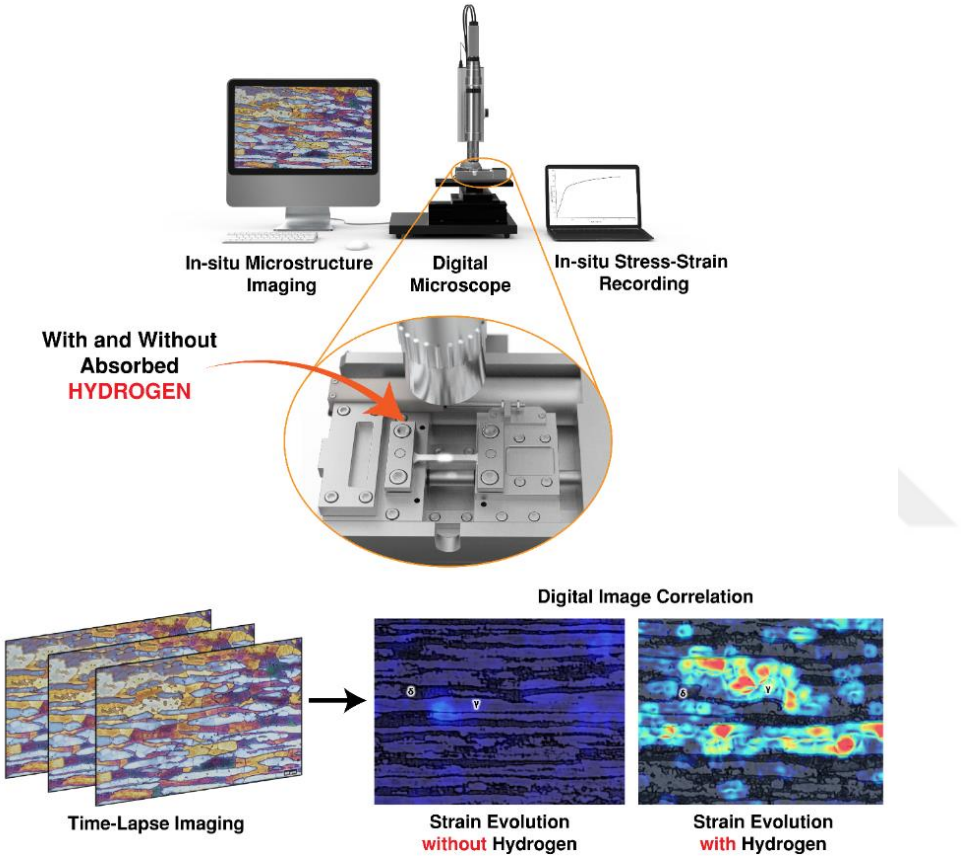

Figure 6.1 : Schematic representation of experimental setup for in-situ micro-tensile testing of hydrogen pre-charged specimens and processing of micrographs with DIC.

6.5 Digital Image Correlation

About 2000 – 3000 images were obtained from the in-situ tensile tests. The images were processed using LaVision DaVis software V10.2.0. The engineering strain tensor mode with the sum of differential correlation mode was used. For the correlation value, the threshold value was chosen as 0.5. The subset size was optimized based on the microstructural pattern and magnification ranging between 20-40 pixels with a step

size of typically a third of the subset size. As a result of discussions with the software developer and experiments, these parameters gave the best values for the DIC. Von Mises strain values were calculated and presented as 2D strain maps.

6.6 In-situ Micro-tensile Testing during Hydrogen Charging

Another form of tensile testing was done to understand the simultaneous effect of hydrogen absorption and mechanical deformation on the susceptibility of the duplex steel to hydrogen embrittlement. For this, two different electrochemical cells were designed: (i) one cell was additively-manufactured, with polylactic acid (PLA) being the printing material, which can be seen in Figure 6.2. The other one was made out of glass (see Figure 6.4).

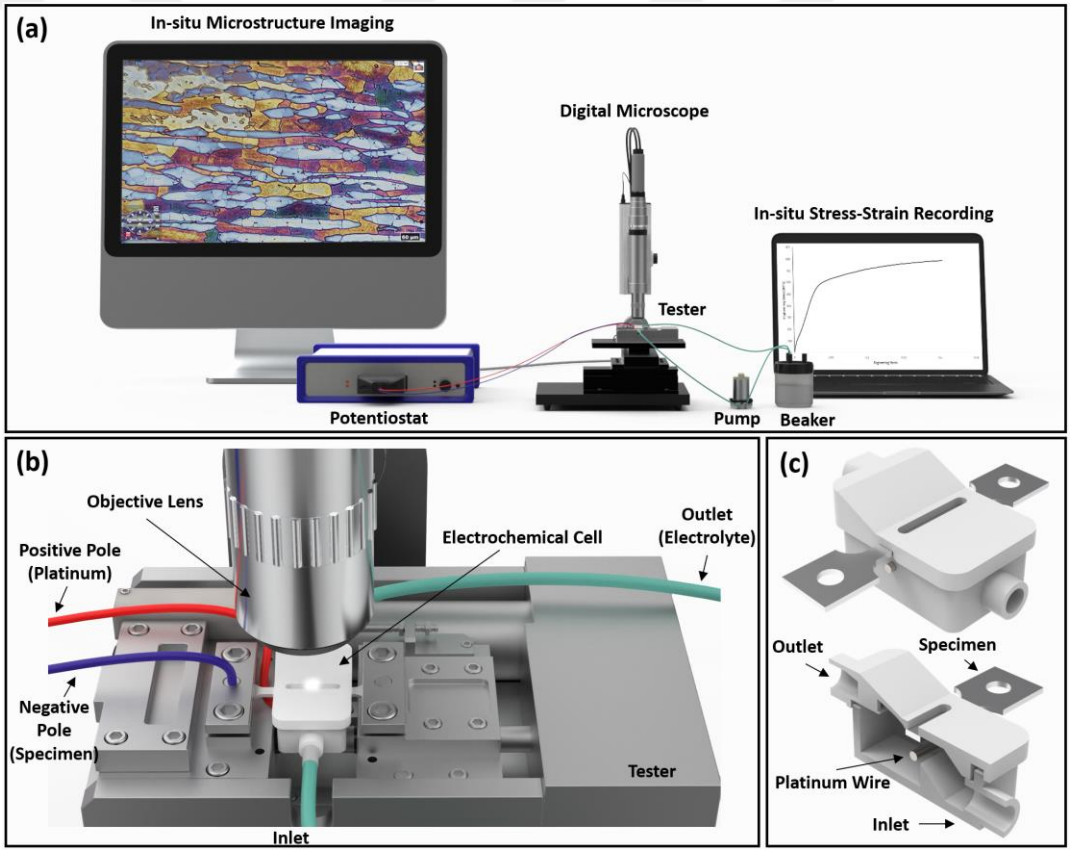

Figure 6.2 : Schematic representation of (a) experimental setup for in-situ micro-tensile testing during hydrogen charging, (b) magnified view of (a), and (c) the 3D-printed electrochemical cell design.

The specimen was mounted on the electrochemical cell and sealed with fast-drying silicone (see Figure 6.3). Then, the assembly was mounted on the tester. The inlet tube was connected to a peristaltic pump which continuously transferred the sodium chloride solution (0.1 M) to the inner compartment of the cell. The pumped electrolyte

exited from the outlet tube back to the same beaker with the pumped electrolyte. Hence, a continuous cycle of pumping was set. The cell was designed so that the formed hydrogen bubbles could easily escape from the outlet tube.

The specimens were hydrogen charged with 38 mA/cm^2 cathodic current density for ten minutes before the tensile test. Then, specimens were strained until fracture with cathodic currents of (i) 4.35 mA/cm^2, (ii) 17 mA/cm^2, and (ii) 38 mA/cm^2 (see Table 6.4).

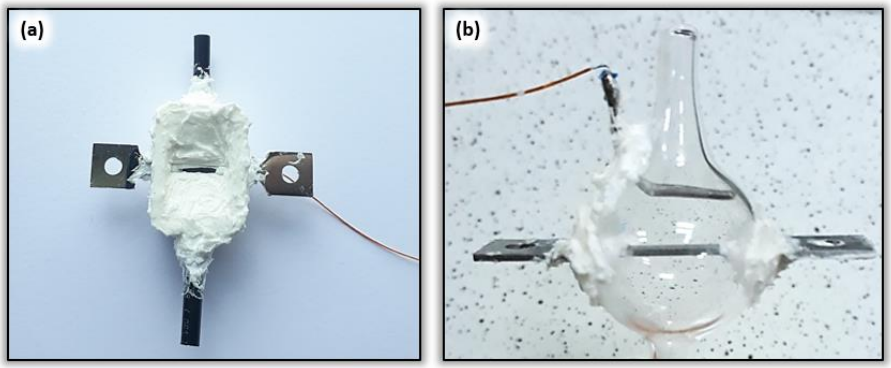

Figure 6.3 : Mounted specimens in (a) additively manufactured and (b) glass electrochemical cells sealed with fast drying silicon. The tensile specimen is 50 mm long.

At the same time, the micrographs from the upper surface of the specimen were continuously recorded with the digital microscope. Thus, the effect of hydrogen on deformation was observed in-situ with the change of microstructure.

With the 3D printed cell, the hydrogen absorption occurs only from the specimen's lower part, allowing in-situ microstructure imaging. Comparing the hydrogen charging times with the pre-hydrogen charged specimens may not be easy since the hydrogen ingress occurred from all sides of the sample for the latter case. The mechanical properties and hence the extent of hydrogen embrittlement will be different. For this reason, a glass electrochemical cell was designed to ensure hydrogen absorption from all sides of the sample while performing in-situ tensile testing (see Figure 6.4). However, in this case, the microstructure cannot be observed.

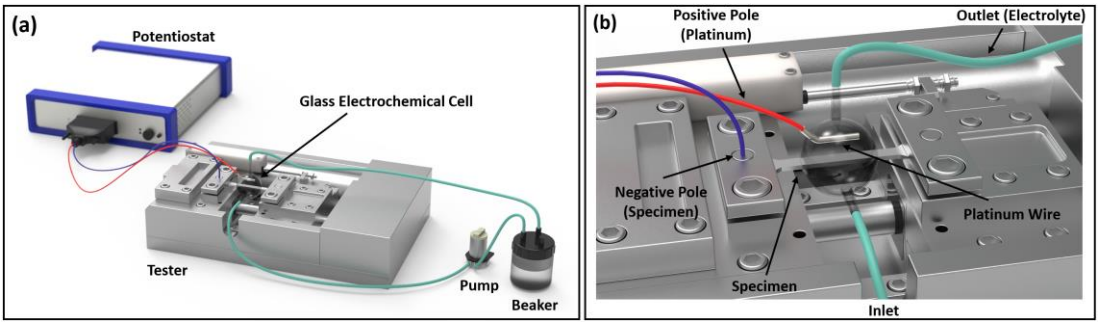

Figure 6.4 : Schematic representation of (a) experimental setup for in-situ micro-tensile testing during hydrogen charging with glass cell and (b) magnified view of (a).

All electrochemical cells were sealed using fast-drying silicone to guarantee no leakage during the deformation experiment. The test conditions of the hydrogen charging during deformation are given in Table 6.4. However, as the specimen was deformed, the specimen elongated in one axis and contracted in the other two axes. Furthermore, the surface roughness changed. Therefore, the surface area did not remain the same, and the current density applied at the beginning also changed. Thus, the current density specified here is the first applied current density value.

Table 6.4 : Experimental conditions for the in-situ micro-tensile tests with in-situ hydrogen charging.

Material	Cathodic Current Density (mA/cm^2)	Time to Fracture	Cell	Magnification	Pixel Resolution
Bar	38 – 17.4[1]	21:14:24	PLA	400x	0.46 µm
Bar	17.4	14:08:46[2]	PLA	400x	0.46 µm
Bar	38	08:13:06	Glass	n.a.[3]	n.a.
Bar	4.34	20:21:01	PLA	200x	0.93 µm

As the amount of deformation increased, it became more difficult to prevent the hydrogen gas adsorption from the surface, and therefore current flow was inhibited. This is the reason for the change in the cathodic current density of the sample fractured in 21 hours. The current density was reduced when the current flow was inhibited to provide hydrogen absorption. A current density of 38 mA/cm^2 was applied during the first 10 hours, up to 11.6 % strain. Then the current density was reduced to 17 mA/cm^2

[1] As the deformation increased, it became more difficult to remove the bubbles formed from the surface and rarely current flow was prevented. Therefore, the current density has been reduced to better control the current flowing.

[2] the experiment was stopped, i.e., the specimen did not fracture

[3] n.a. = not applicable

and applied for two and a half hours until 14.5 % strain. Then the current was cut off. The glass cell did not encounter such a problem because the sample has more surfaces contacting the solution.

6.7 Fractography

To reveal the fracture morphology, selected tensile specimens strained until catastrophic failure were analyzed in a SEM. The details on the fracture surfaces were examined to understand whether the material was ductile fractured (dimples) or brittle fractured (cleavage).

7. RESULTS

7.1 Microstructure

Selected micrographs of the finely-grained and coarsely-grained microstructures, for which the phase fractions and austenite spacings were calculated, are shown in Figure 7.1. The austenite-to-ferrite fractions were in both microstructures at about 50:50. The austenite spacing in finely-grained microstructure was 12 ± 8 µm. The coarsely-grained microstructure had an austenite spacing average of 27 ± 20 µm.

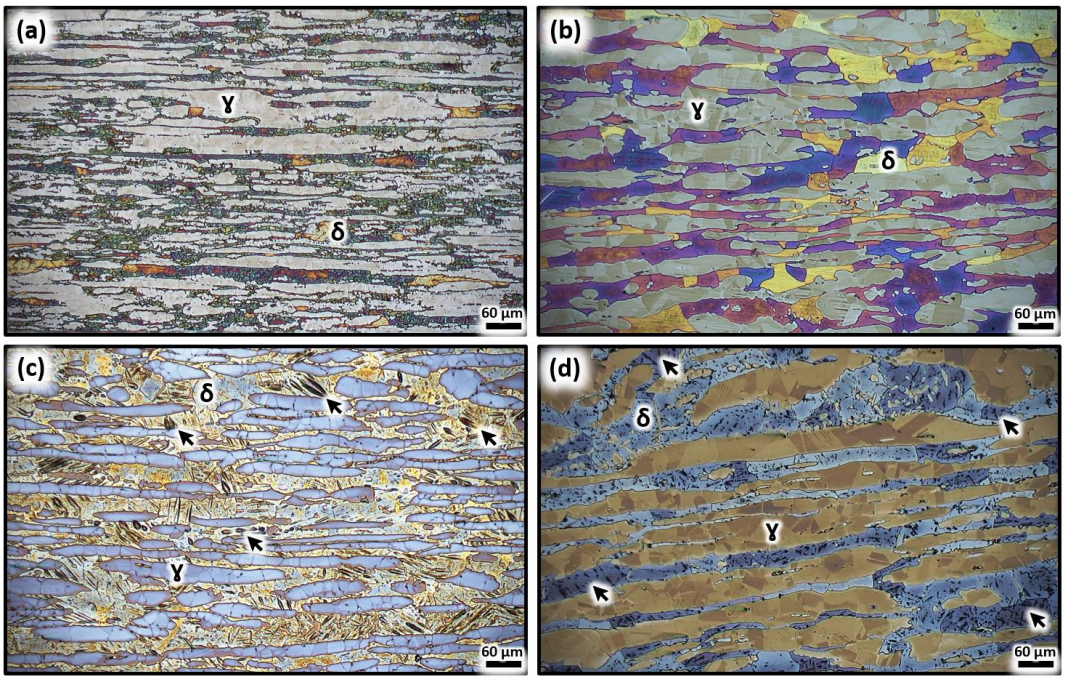

Figure 7.1 : Microstructures of (a) finely-grained SDSS, (b) coarsely-grained SDSS, (c) 10 hours pre-hydrogen charged coarsely-grained SDSS, and (d) 19 days pre-hydrogen charged coarsely-grained SDSS (repolished) and arrows indicate blisters formed in the ferrite phase.

Figure 7.1c and Figure 7.1d show the coarsely-grained microstructures after 10 hours and 19 days of hydrogen charging, respectively. As a result of hydrogen ingress into the material, blister formations were observed in the ferrite phase in the microstructure, as indicated by the arrows in Figure 7.1c and d.

7.2 Effect of Absorbed Hydrogen on the Deformation Behavior

7.2.1 Stress-strain curves

The stress-strain curves of the finely-grained duplex steel as a function of the amount of pre-hydrogen charging are shown in Figure 7.2a. The hydrogen pre-charging increased the yield point and tensile strength with, however, in expense of a reduction of ductility, indicating embrittlement. The elongation of the hydrogen pre-charged sample for 9 days was reduced by almost half. The stress-strain behaviour of the 62-hour charged condition showed no significant embrittlement but hardening. The 9-day (216 hours) charged specimen showed extraordinary deformation characteristics. At around 200 MPa, the specimen began to yield for a minor elongation, followed by a further increase in strength until about 700 MPa when a major yield occurred. Compliance effects of the tester did not cause the minor yielding at 200 MPa. Several tensile tests were carried out. Reproducible results were obtained.

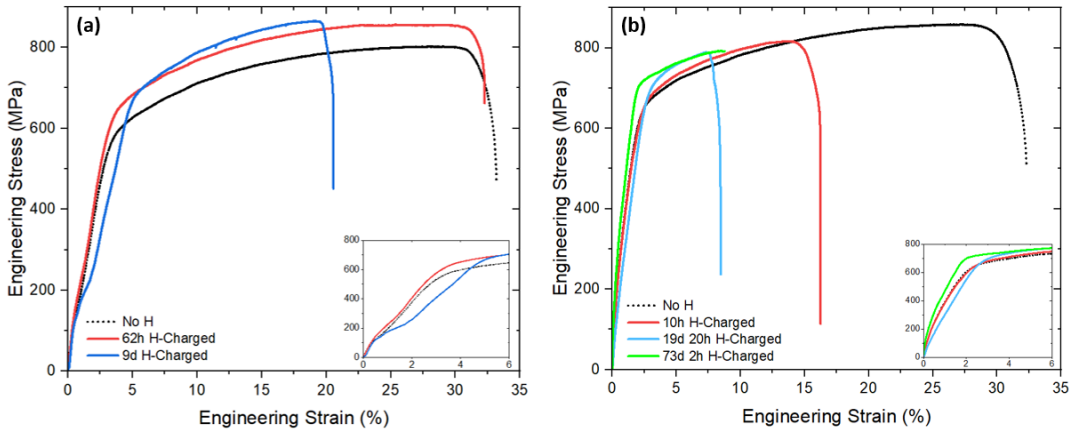

Figure 7.2 : Tensile test results of (a) the finely-grained SDSS tested with 62 hours and 9 days hydrogen charged before the test and (b) the coarsely-grained specimens. The tests began within half an hour after the electrochemical charging process terminated.

Figure 7.2b shows the stress-strain behaviour of the coarsely-grained specimens. Hydrogen charging for 10 hours resulted in severe loss of elongation. The elongation dropped with hydrogen charging time until 6-7% engineering strains after hydrogen absorption for 73 days. There seems to be no difference between charging for 19 days and 73 days.

7.2.2 Deformation characteristics

The microstructure of the finely-grained duplex steel before and after the tensile test under different hydrogen charging conditions is given in Figure 7.3. Figure 7.3a,d,g show the microstructure without absorbed hydrogen. Columns represent no hydrogen (as-received), hydrogen pre-charged for 62 hours, and hydrogen pre-charged for 9 days, respectively. The as-received sample showed necking, indicating ductile fracture (Figure 7.3g). The sample, which was charged with hydrogen for 62 hours, also showed a ductile fracture, while the neck region was slightly smaller. Moreover, large secondary cracks are in the closest vicinity to the central fracture zone. The largest crack is almost 600 µm long. These cracks progressed perpendicular to the tensile direction (Figure 7.3h).

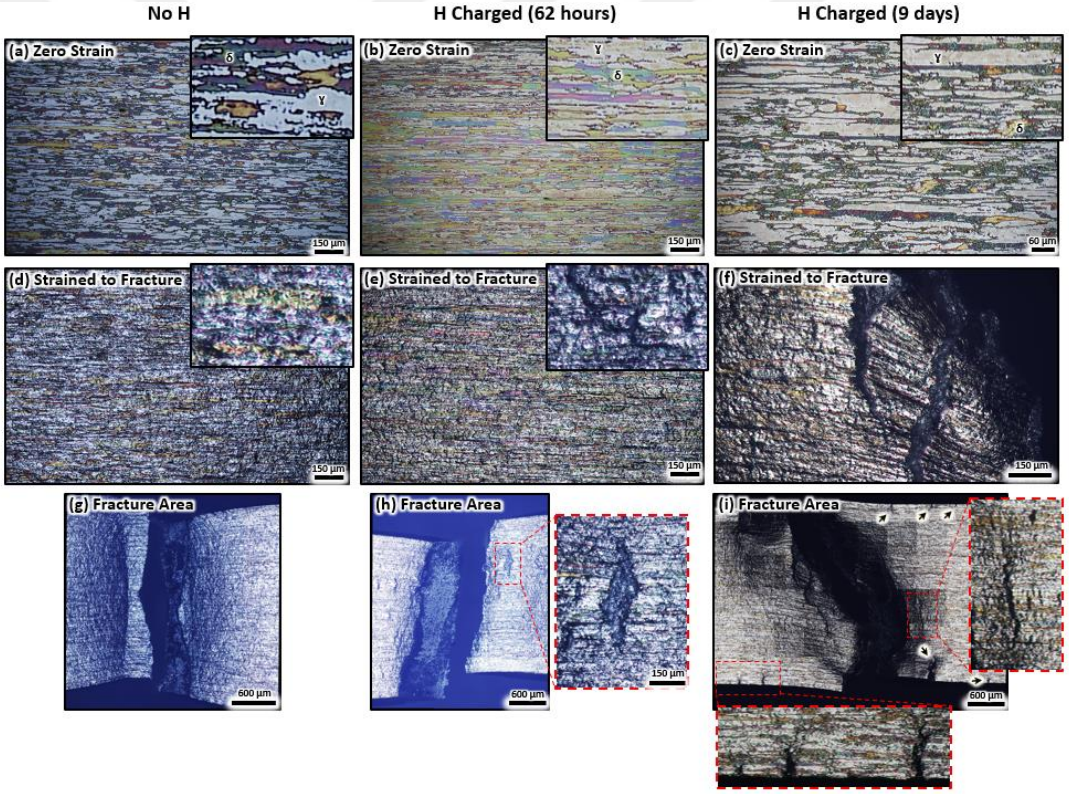

Figure 7.3 : Optical micrographs show the microstructure of the finely-grained SDSS with different pre-hydrogen charging before and after plastic deformation until catastrophic failure. The hydrogen absorption resulted in discrete brittle cracks at and around the necked region.

The 9-day specimen shows no signs of necking which is in line with the stress-strain curves shown in Figure 7.2a. This indicates brittle fracture and hence hydrogen embrittlement. There are, furthermore, severe secondary cracks near the main fracture zone. The length and severity of these secondary cracks are longer than those formed

in the 62-hours sample. In addition, the 9-day specimen showed small cracks at the sample edges (highlighted by arrows in Figure 7.3i). These cracks formed perpendicular to the tensile direction.

Figure 7.4 summarises the deformation behaviour of the coarse microstructure as a function of different hydrogen charging times. The material without hydrogen charging shows no micro-cracks but only severely deformed grains (Figure 7.4a,b,c). Catastrophic failure was due to the formation of a large crack in the gauge-length centre. The material showed major necking indicating ductile fracture behaviour. The 10-hour charged specimen showed hydrogen blisters formed in the ferrite phase, as indicated by the arrows in Figure 7.4d. Upon strain to fracture, dozens of micro-cracks were created around the surface in the vicinity of the main crack (Figure 7.4e). Metallographic re-preparation of the fractured specimen revealed several sub-surface cracks showing that the micro-cracks also initiated inside the microstructure (Figure 7.4f). The cracks primarily developed in and propagated through the ferrite phase and stopped or arrested on austenite grains indicating that embrittlement occurred mainly on the ferrite phase. The austenite phase was still ductile. However, some cracks could also propagate through the small austenite grains.

The 19-days charged microstructure (Figure 7.4g). showed more severe hydrogen blister cracks in the ferrite phase than in the 10-hour charged condition. More prolonged hydrogen charging resulted in more severe brittle micro-crack formation in the ferrite phase, seen on the surface and far deep in the bulk structure (Figure 7.4i). In addition, the number of micro-cracks was higher.

The 79-day charged specimen showed numerous hydrogen-induced micro-cracks in ferrite and the austenite phase (Figure 7.4k). The number of cracks formed in the austenite was higher than in the ferrite. This indicates that the austenite phase also suffered directly from hydrogen embrittlement. In general, the deformation structures are reduced with hydrogen absorption time. Hydrogen reduced the extent of elongation; hence, fewer deformation patterns can be seen in the micrographs (compare Figure 7.4b with Figure 7.4e, Figure 7.4h, and Figure 7.4k).

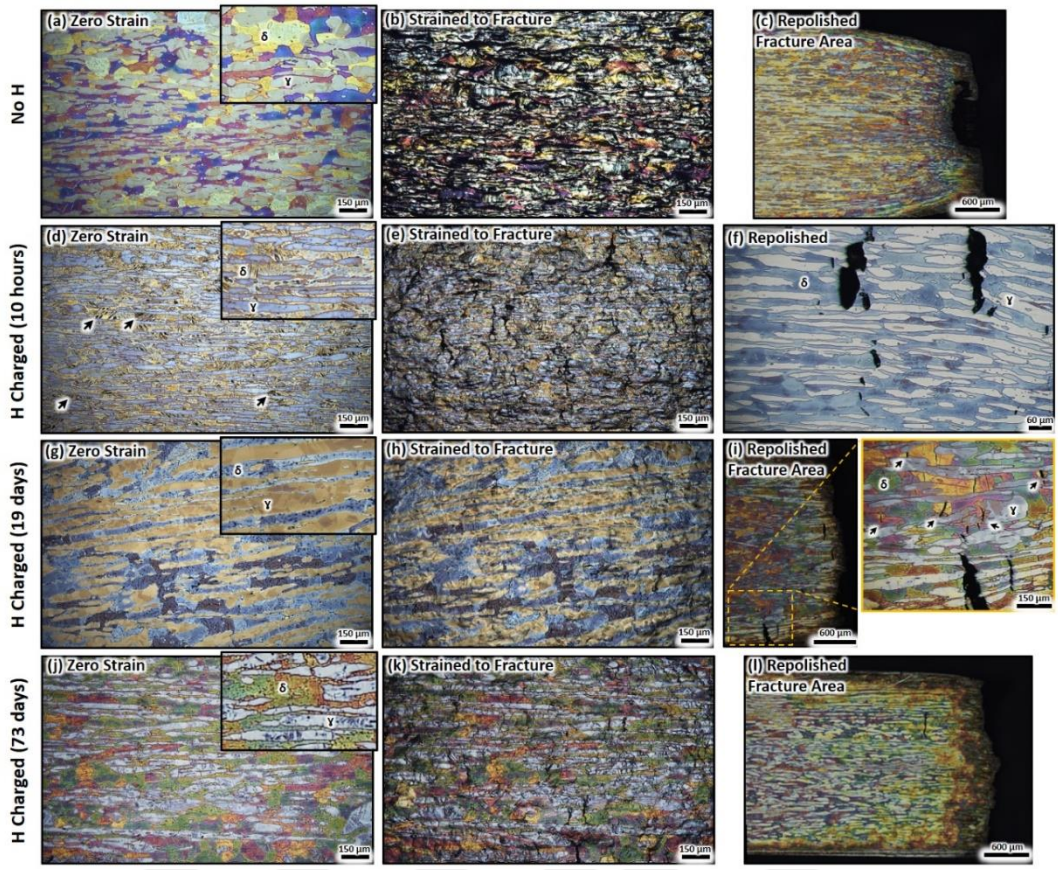

Figure 7.4 : Optical micrographs show the microstructure of the coarsely-grained SDSS with different pre-hydrogen charging before and after plastic deformation until catastrophic failure. The hydrogen absorption resulted in discrete brittle cracks at and around the necked region.

7.2.3 Fracture morphology

The finely-grained SDSS fracture surfaces were investigated by SEM. Figure 7.5 shows the cross-sectional area of the fractured region of the hydrogen-free sample.

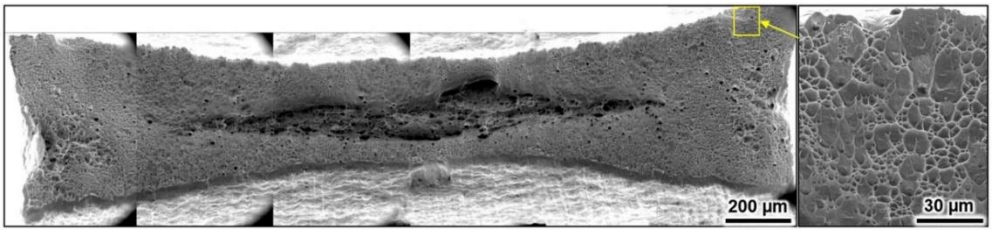

Figure 7.5 : SEM montage micrograph shows the fracture surface of the finely-grained microstructure without hydrogen pre-charging after straining until catastrophic failure.

This SEM image was created by combining several micrographs. Thus, it was imaged over a large area where it could be observed in finer detail. Dimple formations were observed on the fracture surface indicating ductile fracture.

Figure 7.6 shows the cross-sectional fracture areas of the hydrogen pre-charged samples. Brittle cracks and cleavage-like fractures are observed in the regions around the surface of the sample, in the regions of high hydrogen concentration. These are also indicators of brittle fracture. There is also delamination cracking observed due to hydrogen (Figure 7.6a).

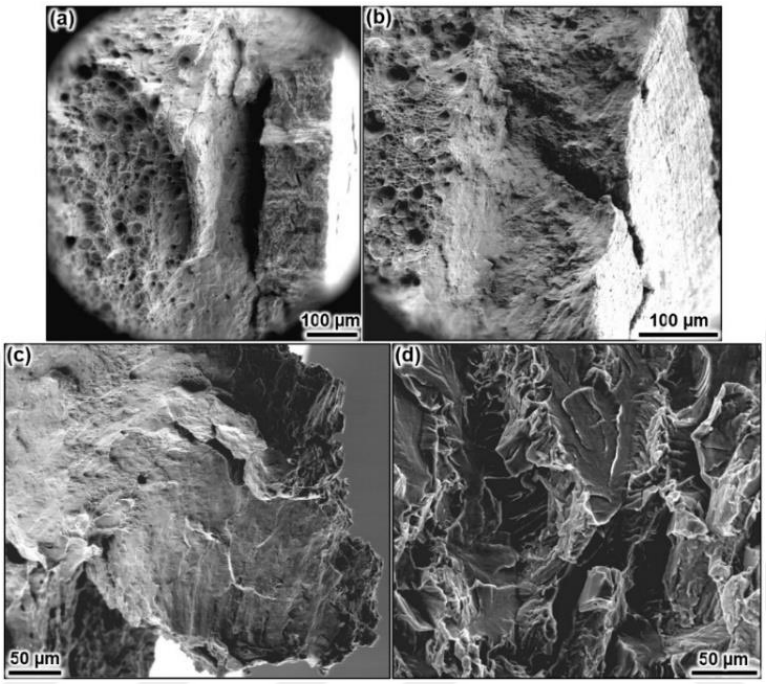

Figure 7.6 : SEM fracture surface of the finely-grained microstructure with hydrogen pre-charging for 9 days after straining until catastrophic failure.

7.3 Effect of Deformation during Hydrogen Charging

As mentioned before, the additively manufactured in-situ cell was designed to see the effect of hydrogen on deformation simultaneously. Figure 7.7 shows images of the upper and bottom surfaces of the in-situ tested specimen with additively manufactured electrochemical cell after the tensile test. The one which is in contact with the solution (bottom surface, see Figure 7.7a), there are substantial secondary cracks because of hydrogen introduction; however, there are no such secondary cracks on the upper surface which is not in contact with the solution (Figure 7.7b).

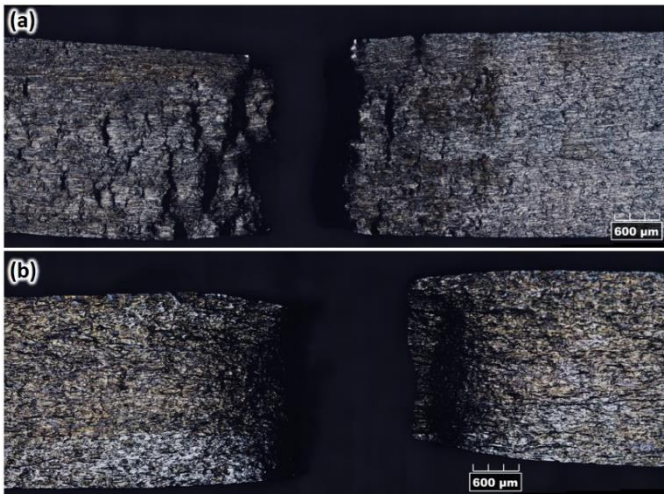

Figure 7.7 : Microstructure images of the coarsely-grained SDSS after in-situ testing using an additively manufactured electrochemical cell: (a) shows the specimen's lower surface that was in contact with the solution and (b) shows the specimen's upper surface that was not in contact with the solution. The upper surface is polished down to 1 µm diamond slurry finish, but the lower surface is ground up to grade 500.

Figure 7.8 shows the repolished microstructure of the coarsely-grained SDSS (Figure 7.7) tested in the 3D-printed cell. When the surface was re-prepared after the tensile test, no secondary cracks were observed in the regions sealed with silicone in places where hydrogen was not charged. In contrast, many secondary cracks were observed on the surfaces of the specimen in contact with the solution. Most of these cracks were formed in the ferrite phase (see Figure 7.8c).

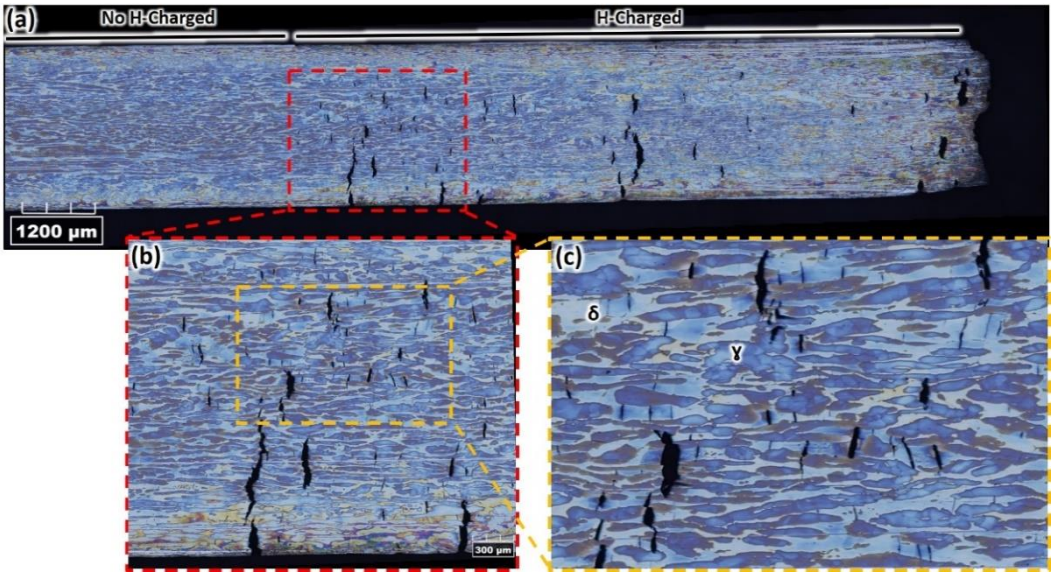

Figure 7.8 : Microstructure images (a) show hydrogen charged and uncharged regions on the repolished specimen after the fracture. (b) shows secondary cracks on ferrite, and (c) is a magnified view of (b).

As can be seen in Figure 7.9, the results of the in-situ tensile test experiments differed compared to the ex-situ experiments. The purple and pink curves are obtained from the in-situ tensile tests. The pink curve was carried out with a 3D-printed cell (PLA), and the purple curve was performed with the glass cell. In the experiment with the glass cell, hydrogen entered from every sample surface. In contrast, hydrogen entered only from the bottom of the 3D-printed cell. Therefore, the effect of this is reflected in the tensile test results. Furthermore, it was seen that hydrogen charging did not increase the strength but instead decreased it.

In-situ hydrogen charging caused a significant decrease in the yield strength, and plastic deformation of the material started at lower strength levels. In addition, when the elastic region was examined, it was observed that hardening occurred compared to the reference sample.

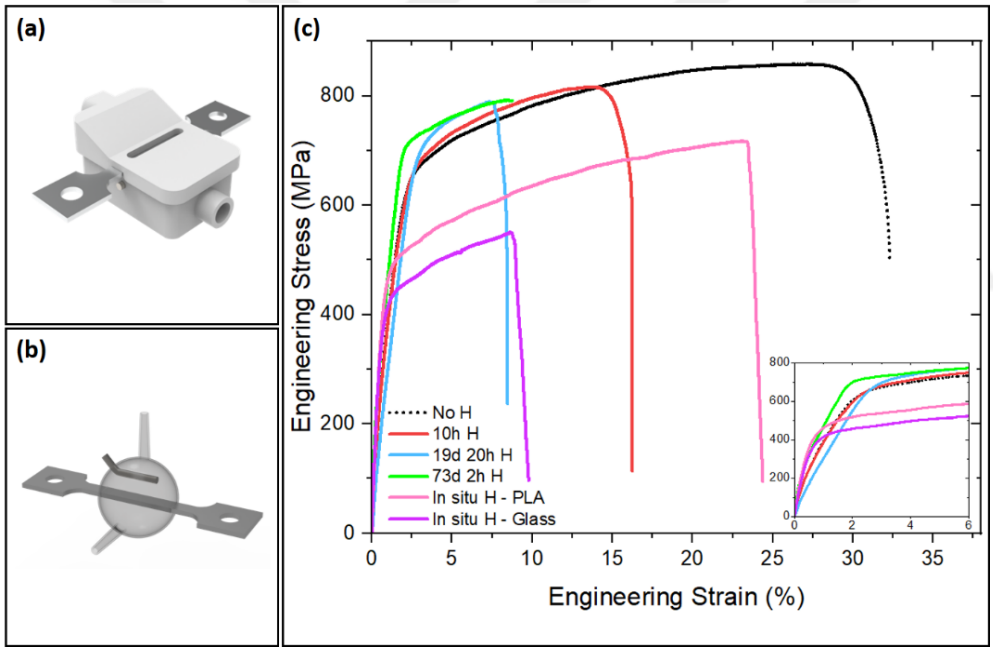

Figure 7.9 : Electrochemical hydrogen charging cells made of (a) PLA and (b) glass used for in-situ tensile straining while simultaneously hydrogen charging. (c) shows the effect of hydrogen absorption time on the mechanical properties of coarsely-grained SDSS.

In contrast, the elongation decreased significantly, indicating hydrogen embrittlement. The green, purple, and pink curves show that hydrogen hardens the microstructure when it is present in high concentrations. The green curve shows the deformation behaviour after excessive charging for 73 days, which saturates the entire specimen with hydrogen. Therefore, the material became stiffer and harder, apparent from the higher yield point. However, the material was embrittled due to a significant reduction

in elongation strain. In-situ straining at in-situ hydrogen charging (purple and pink curves) also resulted in excessive hydrogen uptake because the surface oxide film of the SDSS ruptured continuously, which allowed more efficient hydrogen production and absorption. The surface oxide of stainless steel in the tested electrolyte is spontaneously passive, providing a barrier effect against hydrogen uptake.

Furthermore, oxides are sluggish catalysts in hydrogen production [4], which is good for resisting hydrogen embrittlement, but hydrogen is far less efficiently formed than bare metal. Moreover, the oxide is brittle compared to the bulk steel microstructure, and during tensile straining, it breaks. Hence, hydrogen can be produced directly on bare metal parts and easily infuse the material interior.

7.4 Digital Image Correlation

The DIC results of the tube material are given in Figure 7.10, Figure 7.11, Figure 7.12, and Figure 7.13. Only two sections from the DIC analysis are presented. These are data at stress values of 200 MPa and 600 MPa. The 600 MPa value is given because it represents the approximate yield point, and 200 MPa represents the point of early microplasticity (see Figure 7.2a).

In Figure 7.10, it is seen that there is no severe deformation at 200 MPa and the resulting deformation is homogeneous. However, at 600 MPa, it was observed that the amount of strain increased in several regions, and these regions were on austenite.

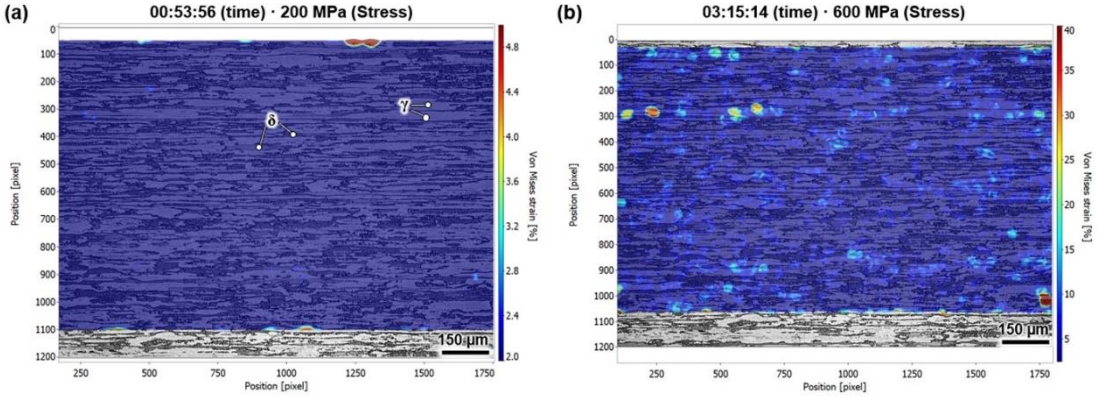

Figure 7.10 : DIC results of the finely-grained specimen without hydrogen showing microstrain evolution at a tensile load of (a) 200 MPa and (b) 600 MPa.

The microstructure charged with hydrogen for 62 hours (Figure 7.11) showed the evolution of numerous strain hot spots. The strain maps show that local plastic

deformation occurred already in the macro-elastic regime. More strain hot spots were formed with higher intensities at a tensile load of 600 MPa, developing primarily in the austenite phase.

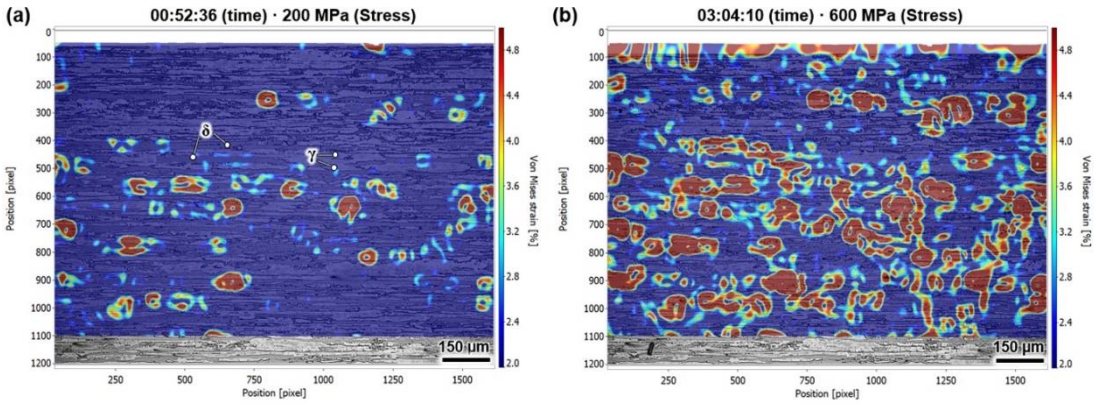

Figure 7.11 : DIC results of finely-grained specimen hydrogen charged for 62 hours showing microstrain formation at a tensile load of (a) 200 MPa and (b) 600 MPa.

The number and magnitude of the strain hot spots increased with pre-hydrogen charging, which can be seen on the sample charged with hydrogen for 9 days (Figure 7.12). The strain became more localized in austenitic grains. The strain in large austenite grains was higher than in smaller grains.

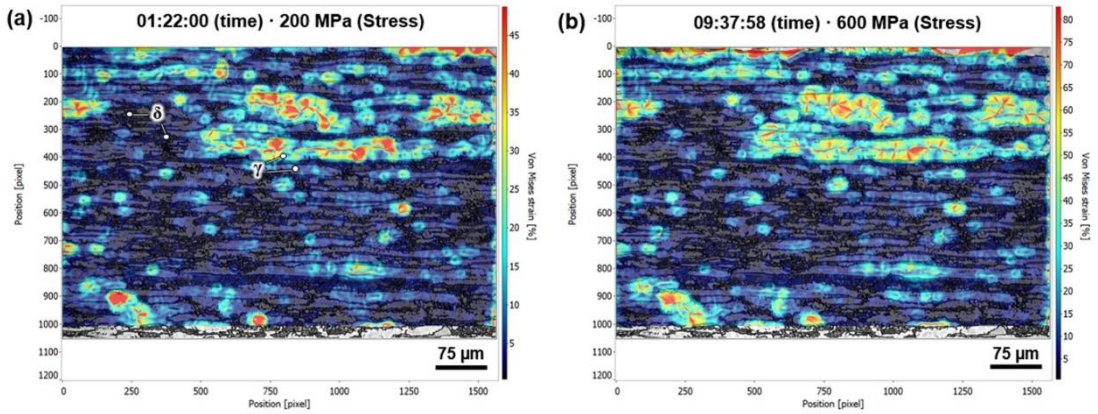

Figure 7.12 : DIC results of the finely-grained microstructure hydrogen charged for 9 days showing microstrain evolution during tensile loading at (a) 200 MPa and (b) 600 MPa.

The strain pattern varied from grain to grain, showing large variations across the microstructure (Figure 7.13). The DIC results revealed the path of material flow. Plastic strain set on at interphase regions and directed towards the grain centre of the austenitic grains.

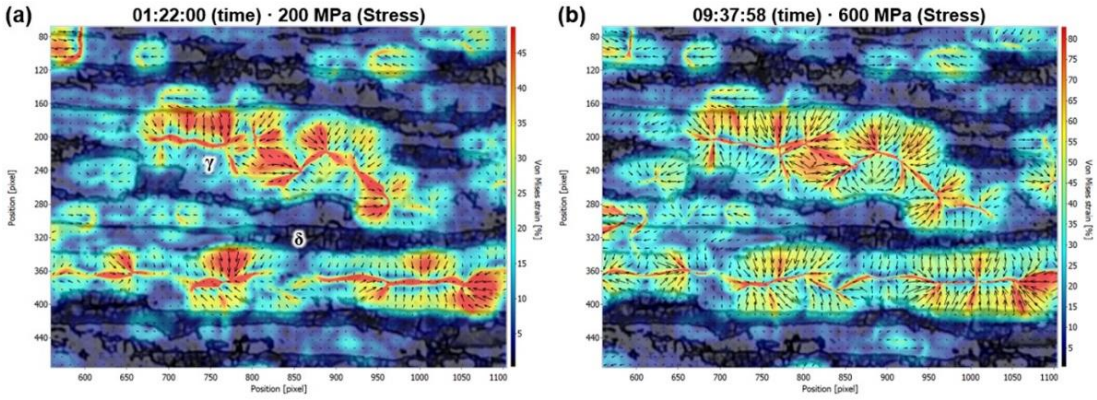

Figure 7.13 : DIC results of the finely-grained microstructure hydrogen charged for 9 days showing microstrain evolution with a high resolution during tensile straining at a load of (a) 200 MPa and (b) 600 MPa.

Figure 7.14 summarizes the DIC results of the experiments conducted with the coarsely-grained microstructure. Only three excerpts are shown at (i) 300 MPa, (ii) 670 MPa, and (iii) 730 MPa, corresponding to (i) elastic, (ii) early plastic, and (iii) far plastic regimes (see Figure 7.2b).

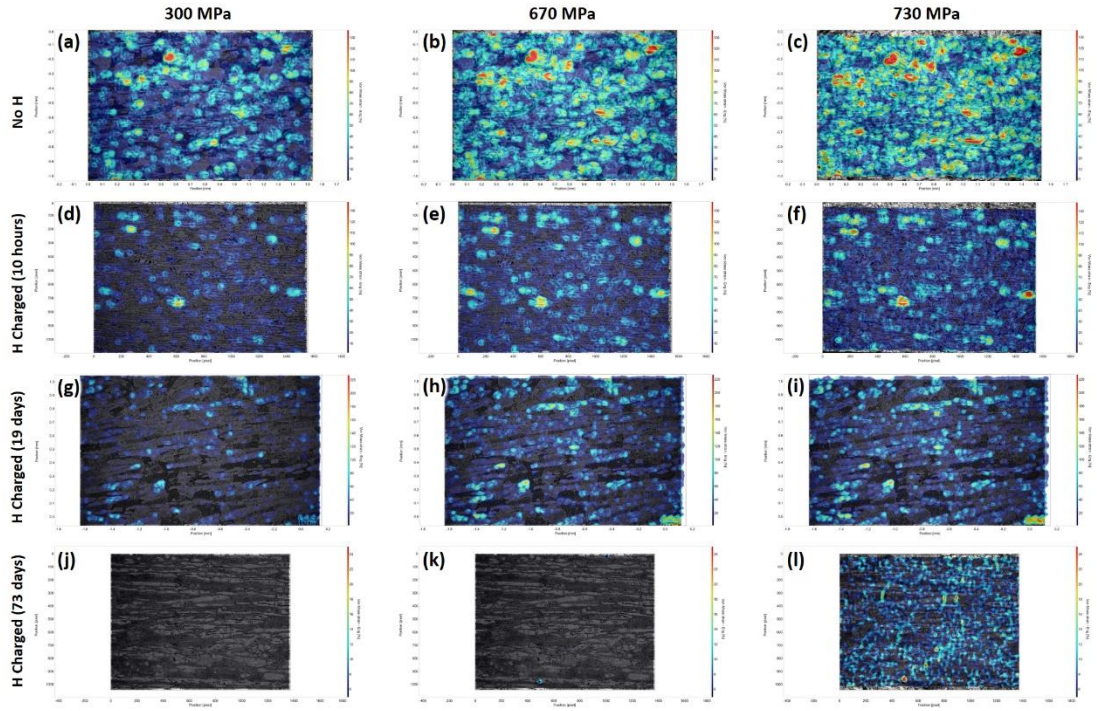

Figure 7.14 : DIC results of no hydrogen, 10 hours, 19 days, and 73 days hydrogen charged coarsely-grained specimen at (i) 300 MPa, (ii) 670 MPa, and (iii) 730 MPa.

Without hydrogen, the strains localized in a few austenitic areas. With increasing plastic deformation, more strains formed in austenite and ferrite grains. The strains in the austenite phase were higher than in the ferrite phase (Figure 7.14a,b,c).

Hydrogen charging caused a more discretization of the strain formation. This can be seen in the hydrogen-charged specimens. The total strain area was reduced with increasing hydrogen charging time and concentrated more favourably on austenite grains. In the 73 hydrogen-loaded microstructure, there is a severe increase in hardness compared to the sample that does not contain hydrogen. No severe deformation was observed in the sample at 300 MPa and 670 MPa. Deficient strains were observed at 730 MPa (Figure 7.14j,k,l). However, the orientations of these strains are perpendicular to the tensile direction. Although minimal deformation was observed locally, cracks in the austenite phases were triggered by ferrite cracking and crack propagation. While crack formations were observed in the ferrite phase in other samples, large cracks were seen in the austenite phases here (Figure 7.15).

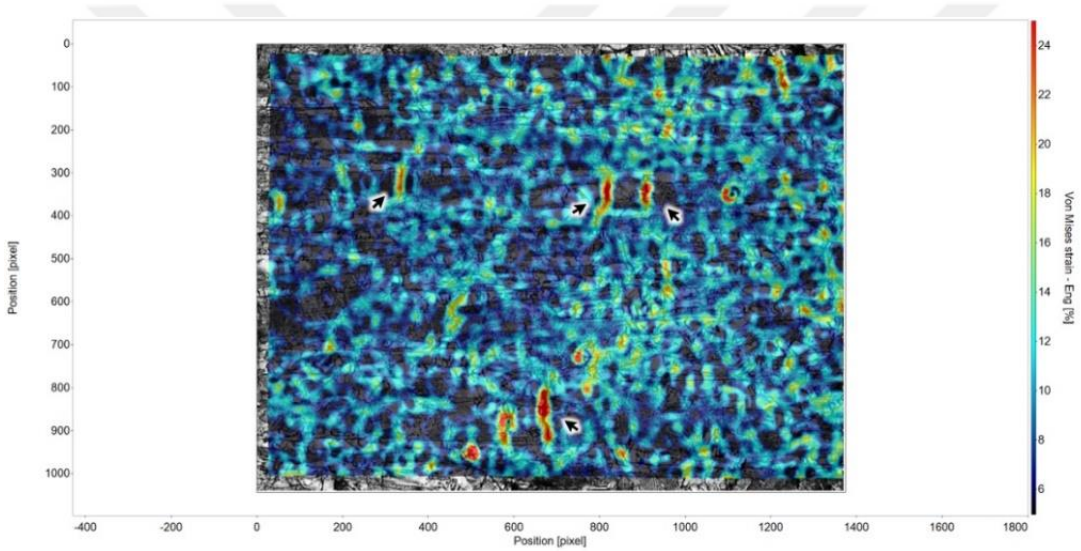

Figure 7.15 : DIC results of coarsely-grained microstructure hydrogen charged for 73 days showing microstrain evolution during tensile load at 753 MPa. The arrows indicate cracks.

Figure 7.16 shows the result of the in-situ experiment tested with the 3D-printed cell (hydrogen charging only from one side). Here, 300 MPa is chosen to represent the elastic region and 625 MPa to describe the plastic area. In-situ straining with in-situ hydrogen charging caused strain localization all over the microstructure. The strains formed at interphase boundaries and in austenite and ferrite grains in proportional amounts. In contrast to the previous tests, the strains were relatively homogeneous, indicating that in-situ straining with simultaneous hydrogen charging provokes strain localization all over the microstructure.

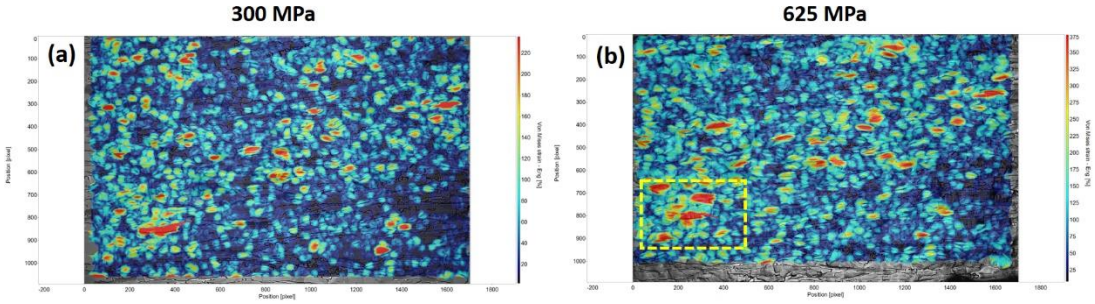

Figure 7.16 : DIC results of coarsely-grained microstructure strained during simultaneous hydrogen charging. Strain formation occurred homogeneously all over the microstructure.

Figure 7.17 gives a closer view of the DIC analysis and the relevant part of the microstructure before deformation. In the in-situ tensile testing and hydrogen loading experiment, it was observed that hydrogen intensifies the strain in ferrite, austenite and phase boundaries.

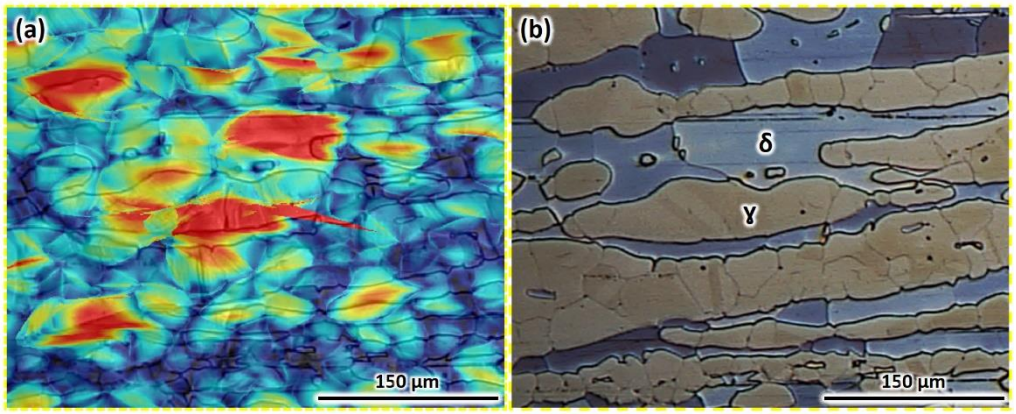

Figure 7.17 : Magnified view of yellow square region in Figure 7.16. (a) Strain mapping of microstructure with DIC and (b) microstructure of in-situ tested super duplex stainless steel before deformation.

8. DISCUSSION

The stress-strain measurements have shown characteristics associated with hydrogen charging and the microstructure. For example, changes in the yield point, tensile strength, Young's modulus, elongation to fracture, and the curve shape of the elastic-to-plastic transition were seen. Furthermore, these changes differed between the studied microstructures.

The yield point of the fine microstructure increased with hydrogen charging time, indicating hydrogen-induced hardening. However, 62 hours of charging showed no apparent embrittlement. Seemingly, the fine microstructure showed improvement in toughness. The austenite can accommodate 100-times higher solubility than the ferrite. Phase and grain boundaries are typically the most potent sites for hydrogen trapping. Hence, the smaller the microstructure, the more hydrogen can be accommodated/trapped. It seems that after 62 hours of hydrogen charging, the fine microstructure was not affected by the absorbed hydrogen, suggesting that the trap sites were not fully occupied. It can be concluded that as long as trap sites exist, the material has sufficient resistance to hydrogen embrittlement. This hypothesis is in line with the thoughts of Bhadeshia, who stated that only mobile hydrogen is detrimental and that immobilized hydrogen atoms are innocuous to the material [4].

The DIC results (Figure 7.12 and Figure 7.13) showed that a significant increase in plastic strain occurred in the austenite phase already in the macroscopic elastic regime at 200 MPa, which indicated microplasticity. This observation explains the unusual stress-strain behavior in Figure 7.2a. Hence, hydrogen absorption resulted in softening of the austenite phase. However, the stress-strain curve in Figure 7.2a shows a macroscopic rise in the yield strength due to hydrogen ingress. Therefore, this must indicate that the ferrite has hardened. On the other hand, the DIC results have demonstrated that the ferrite phase deformed less than the austenite phase, supporting the earlier statement. So, one can say that the fine microstructure after 9 days of hydrogen charging got two yield points. Macroscopically, the microstructure softened due to early plasticity observed in the austenite phase at around 200 MPa. But the

ferrite hardened and increased the yield point to higher values of approximately 700 MPa.

Softening and hardening due to hydrogen are well documented in the literature. Softening is explained by enhanced dislocation activity, which is more favored in the austenite phase. Dislocations can be easier activated and moved at slip planes. Hardening is explained by dislocation pinning. It remained not entirely understood why the hydrogen pins the dislocations in the ferrite but facilitates those in the austenite. It is certain that hydrogen increases the Peierls stress in the ferrite but reduces it in the austenite phase. This explanation is also valid for the coarse microstructure.

The yield point of the coarse microstructure also increased with hydrogen charging. However, the rise of the flow stress was less than the fine microstructure. This observation supports the trapping theory stating that immobilized hydrogen increases the material strength due to reduced dislocation mobility, similar to precipitation hardening. The more trapping, the more hardening, which explains why the fine microstructure showed more rise in strength.

Young's modulus was seen to change with hydrogen absorption. The changes in the modulus mean that the atomic bonding energy has changed, typically due to chemical effects. Hydrogen absorption is forced chemical alloying or may be considered decontamination. The coarse microstructure showed changes in modulus. It was seen that the microstructure became softer and stiffer. This behavior is not understood and shall not be explained in this thesis. Interestingly, the coarse microstructure is stiffer than the fine microstructure.

Moreover, hydrogen diffusion in large ferrite grains occurs less hindered due to less tortuosity. Hydrogen diffusion is higher in the ferrite ($D_\delta = 1.5\ x\ 10^{-5}\ \frac{m^2}{sec}$) than the austenite ($D_\gamma = 1.4\ x\ 10^{-10}\ \frac{m^2}{sec}$). The size and morphology of the ferrite grains dictate the preferred hydrogen diffusion path in duplex microstructures. However, the hydrogen solubility in the austenite phase is higher. Therefore, the size, fraction and distribution of the austenite grains determine how much hydrogen can be trapped.

Birnbaum et al. demonstrated [16] that the movement of dislocations increased when hydrogen was introduced into aluminum and austenitic stainless steel. The dislocations

were seen to pile up at grain boundaries, and when no further hydrogen was introduced, the dislocations reversed to their original locations in aluminum. In contrast, the dislocations only stopped moving in austenitic stainless steel. It was explained that the alloy nature of stainless steel is the reason for dislocation inactivity. Chemical heterogeneity causes dislocation pinning, which for aluminum is not the case. However, it remained not understood whether hydrogen effuses out from both materials. The differences in hydrogen solubility could also explain these differences. The hydrogen solubility of austenitic stainless steel is orders of magnitude higher than in aluminum. Upon termination of hydrogen ingress in aluminum causes more rapid hydrogen outflow, resulting in reversed dislocation motion. It should be noted that stagnant dislocations may not necessarily mean embrittlement. Delayed or more difficult dislocation activity could also mean hardening, which has been seen for the fine microstructure.

The dislocation pinning effect could also be hearkened back to the coarse microstructure, which showed less strain hardening and more embrittlement than the fine microstructure.

On the other hand, how much hydrogen can diffuse out from ferrite at this time is found as 164 μm if it is calculated according to the second Fick's law ($x = \sqrt{D \cdot t}$) and Mente's [41] diffusion coefficient ($1.5 \times 10^{-5}\ \frac{m^2}{sec}$). Ferrite forms the matrix and has a continuous structure. So, the diffusion occurs primarily through the ferrite phase with a tortuous path due to austenite islands embedded in the ferrite phase. However, since the austenite spacing is small, the hydrogens in some ferrite grains can diffuse into austenite or at the grain boundary. Therefore, the increased dislocation mobility during hydrogen loading may cause the dislocations to remain in place later on and delay the plastic deformation of the ferrite since dislocation movement becomes more difficult if we consider the thoughts of Birnbaum. This can cause an increase in yield strength. When the surface was examined after the tensile test, secondary cracks were observed in the ferrite. While the ferrite fractured brittle, the cracks stopped at the austenite boundary. The crack continued in small austenite grains.

There is slight strain formation in the hydrogen pre-charged specimen for 73 days. However, crack formations were also seen in austenite, triggered by the crack formation in the ferrite phase as it continued to deform. This is because some austenite

grains are fully saturated. Thus, a higher hydrogen amount leads to a change in the hydrogen embrittlement mechanism. For example, *Zhang et al.* [50] show that when hydrogen amount increases, the mechanism change from HELP to HEDE.

However, in-situ tensile testing and hydrogen charging experiments showed a transition to plastic deformation earlier than yield strength. This is because the dislocation mobility and nucleation have increased due to the hydrogen ingress. Furthermore, the DIC results showed strain to grow in ferrite and austenite. Therefore, hydrogen increases dislocation mobility, and an early transition to plasticity was observed—afterwards, early crack formation and fracture due to hydrogen-induced deformation localization.

9. CONCLUSION

Ex-situ tensile testing and microstructure imaging experiments were done to finely-grained and coarsely-grained SDSSs. Then, cracks were investigated by repolishing specimens surface to indicate where cracks occured and propagated. In-situ tensile testing and hydrogen charging experiment, and simultaneously microstructure imaging were performed. The same procees to reveal cracking behavior were conducted. DIC procedure was realized to investigate microstructure constituents behavior with the effect of hydrogen and as-received. To sum up, there are essential implications:

- Ex-situ hydrogen charging increases the strength of the microstructure, while in-situ hydrogen charging decreases the strength of the microstructure. Plastic deformation starts earlier than yield strength.
- Ductility decreases in both charging conditions.
- There is a significant decrease in toughness by in-situ hydrogen charging.
- Ex-situ experiments showed an increase in strength and a decrease in ductility as the hydrogen charging time increased.
- Ex-situ experiments showed that austenite softened with hydrogen loading while ferrite hardened. However, softening was observed in both phases in in-situ experiments.
- In ex-situ experiments, embrittlement of austenite was also observed in specimens loaded with hydrogen for a long time (73 days).
- In in-situ experiments, significant strain formations were observed at the grain boundaries between the ferrite-austenite and in both phases.
- While diffusing hydrogen caused softening of both phases, the trapped hydrogen caused hardening.
- Smaller austenite spacing microstructure is more resistant to hydrogen embrittlement.
- Hydrogen increased local strain heterogeneity.

10. FUTURE WORKS

The cell design for experimental setup is open to improvement. When the designed in-situ electrochemical cell, PLA, is not well sealed with silicon by user, solution leaks may occur after excessive deformation in materials with high ductility. To prevent this, the design will be improved. By using polyether ether ketone (PEEK) (more durable) instead of PLA, the electrochemical cell will be developed by screwing from the edges. The cell can also be developed for later use in SEM. Then, by using it together with micro printing, experiments such as where the hydrogen egress when there is no deformation and where it releases during the deformation can be performed, and comments on hydrogen permeation can be made. It can also be combined with techniques such as scanning kelvin probe force microscopy (SKPFM).

By using electrochemical cells inside SEM, changes in dislocation density and mobility can be observed separately in austenite and ferrite phases in in-situ experiments with SEM-based detectors such as electron backscatter diffraction (EBSD) and ECCI. Thus, the hydrogen embrittlement of SDSS can be better understood with the results obtained from several combined methods.

REFERENCES

[1] **Crabtree, G. W., Dresselhaus, M. S., and Buchanan, M. V.** (2004). The hydrogen economy, *Phys. Today*, **57**, 39–44.

[2] **Raabe, D., Tasan, C. C., and Olivetti, E. A.** (2019). Strategies for improving the sustainability of structural metals, *Nature*, **575**, 64–74.

[3] **Ma, Y., Souza, I. R., Bai, Y., Schenk, J., Patisson, F., Beck, A., …. Raabe, D.** (2022). Hierarchical nature of hydrogen-based direct reduction of iron oxides, *Scr. Mater.*, **213**. doi: 10.1016/j.scriptamat.2022.114571.

[4] **Bhadeshia, H. K. D. H.** (2016). Prevention of Hydrogen Embrittlement in Steels, *ISIJ Int.*, **56**, 24–36.

[5] **Lynch, S. P.** (2011). Hydrogen embrittlement (HE) phenomena and mechanisms, *Stress Corros. Crack. Theory Pract.*, 90–130.

[6] **Olsson, J., and Snis, M.** (2007). Duplex - A new generation of stainless steels for desalination plants, *Desalination*, **205**, 104–113.

[7] **Liang, X. Z., Zhao, G. H., Dodge, M. F., Lee, T. L., Dong, H. B., and Rivera-Díaz-del-Castillo, P. E. J.** (2020). Hydrogen embrittlement in super duplex stainless steels, *Materialia*, **9**.

[8] **Johnson, W. H.** (1875). On Some Remarkable Changes Produced in Iron and Steel by the Action of Hydrogen and Acids, *R. Soc.*, **23**, 168–179.

[9] **Barrera, O., Bombac, D., Chen, Y., Daff, T. D., Galindo-Nava, E., Gong, P., …. Sweeney, F.** (2018). Understanding and mitigating hydrogen embrittlement of steels: a review of experimental, modelling and design progress from atomistic to continuum, *J. Mater. Sci.*, **53**, 6251–6290. doi: 10.1007/s10853-017-1978-5.

[10] **Pfeil, L. B.** (1926). The effect of occluded hydrogen on the tensile strength of iron, *Proc. R. Soc. London. Ser. A*, **112**, 182–195.

[11] **Troiano, A. R.** (2016). The Role of Hydrogen and Other Interstitials in the Mechanical Behavior of Metals, *Metallogr. Microstruct. Anal.*, **5**, 557–569.

[12] **Oriani, R. A.** (1972). A Mechanistic Theory of Hydrogen Embrittlement of Steels, *Technol. Asp.*, **76**, 848–857.

[13] **Beachem, C. D.** (1972). A new model for hydrogen-assisted cracking (hydrogen "embrittlement"), *Metall. Trans.*, **3**, 441–455.

[14] **Birnbaum, H. K.** (1989). Mechanics of Hydrogen related Fracture of Metals, *Acta Metall.*, **37**, 1407–1413.

[15] **Birnbaum, H. K., and Sofronis, P.** (1994). Hydrogen-enhanced localized plasticity-a mechanism for hydrogen-related fracture, *Mater. Sci. Eng. A.*, **176**, 191–202.

[16] **Ferreira, P. J., Robertson, I. M., and Birnbaum, H. K.** (1998). Hydrogen effects on the interaction between dislocations, *Acta Mater.*, **46**, 1749–1757.

[17] **Lynch, S. P.** (1988). Environmentally assisted cracking: Overview of evidence for an adsorption-induced localised-slip process, Acta Metall., **36**, 2639–2661.

[18] **Örnek, C., Larsson, A., Harlow, G. S., Zhang, F., Kroll, R., Carlà, F., …. Pan, J.** (2020). Metastable precursor structures in hydrogen-infused super duplex stainless steel microstructure – An operando diffraction experiment, *Corros. Sci.*, **176**. doi: 10.1016/j.corsci.2020.109021.

[19] **Nagumo, M.** (2001). Function of hydrogen in embrittlement of high-strength steels, *ISIJ Int.*, **41**, 590–598.

[20] **Nagumo, M.** (2004). Hydrogen related failure of steels - A new aspect, *Mater. Sci. Technol.*, **20**, 940–950.

[21] **Kirchheim, R.** (2009). On the solute-defect interaction in the framework of a defactant concept, *Int. J. Mater. Res.*, **100**, 483–487.

[22] **Kirchheim, R.** (2007). Reducing grain boundary, dislocation line and vacancy formation energies by solute segregation. II. Experimental evidence and consequences, *Acta Mater.*, **55**, 5139–5148.

[23] **Kirchheim, R.** (2007). Reducing grain boundary, dislocation line and vacancy formation energies by solute segregation. I. Theoretical background, *Acta Mater.*, **55**, 5129–5138.

[24] **Nilsson, J. O.** (1992). Super duplex stainless steels, *Mater. Sci. Technol.*, **8**, 685–700.

[25] **Callister, J. W. D., and Rethwisch, D. G.** (2014). *Materias Science and Engineering: An Introduction* (9th ed.).

[26] **Abbaschian, R., Abbaschian, L., and Reed-Hill, R.** (2009). *Physical Metallurgy Principles*.

[27] **Dieter, G. E.** (1988). *Mechanical Metallurgy*. London: McGraw-Hill.

[28] **Koyama, M., Rohwerder, M., Tasan, C. C., Bashir, A., Akiyama, E., Takai, K., …. Tsuzaki K.** (2017). Recent progress in microstructural hydrogen mapping in steels: quantification, kinetic analysis, and multi-scale characterisation, *Mater. Sci. Technol.*, **33**, 1481–1496. doi: 10.1080/02670836.2017.1299276.

[29] **D. Rudomilova, D., Prošek, T., and Luckeneder, G.** (2018). Techniques for investigation of hydrogen embrittlement of advanced high strength steels, *Corros. Rev.*, **36**, 413–434.

[30] **Chai, G., Ronneteg, S., Kivisäkk, U., Peng, R. L., and Johansson, S.** (2009). Mechanisms of hydrogen induced stress crack initiation and propagation in super duplex stainless steels, *Steel Res. Int.*, **80**.

[31] **Oltra, R., Bouillot, C., and Magnin, T.** (1996). Localized hydrogen cracking in the austenitic phase of a duplex stainless steel, *Scr. Mater.*, **35**, 1101–1105.

[32] **Örnek, C., Müller, T., Kivisäkk, U., Zhang, F., Långberg, M., Lienert, U., …. Pan, J.** (2020). Operando time- and space-resolved high-energy X-ray diffraction measurement to understand hydrogen-microstructure interactions in duplex stainless steel, *Corros. Sci.*, **175**. doi: 10.1016/j.corsci.2020.108899.

[33] **Kim, J., Tasan, C. C.** (2019). Microstructural and micro-mechanical characterization during hydrogen charging : An in situ scanning electron microscopy study, *Int. J. Hydrogen Energy.*, **44**, 6333–6343.

[34] **Koyama, M., Taheri-Mousavi, S.M., Yan, H., Kim, J., Cameron, B. C., Moeini-Ardakani, S. S., …. Tasan, C. C.** (2020). Origin of micrometer-scale dislocation motion during hydrogen desorption, *Sci. Adv.*, **6**. doi: 10.1126/sciadv.aaz1187.

[35] **Meyers, M., and Chawla, K.** (2009). *Mechanical Behavior of Materials* (2nd ed.). Cambridge: Cambridge University Press.

[36] **Marcus, P.** (2011). *Corrosion Mechanisms in Theory and Practice* (3rd ed.). Boca Raton: CRC Press.

[37] **Turnbull, A.** (2012). Gaseous Hydrogen Embrittlement of Materials in Energy Technologies Mechanisms, Modelling and Future Developments. Gangloff, R. P., and Somerday, B. P. (Eds.), *Hydrogen diffusion and trapping in metals* (Vol. 1, pp.89-128). Oxford: Woodhead Publishing Limited.

[38] **Senöz, C., Evers, S., Stratmann, M., and Rohwerder, M.** (2011). Scanning Kelvin Probe as a highly sensitive tool for detecting hydrogen permeation with high local resolution, *Electrochem. Commun.*, **13**, 1542–1545.

[39] **Chen, Y. S., Lu, H., Liang, J., Rosenthal, A., Liu, H. Sneddon, G., …. Cairney, J. M.** (2020). Observation of hydrogen trapping at dislocations, grain boundaries, and precipitates, *Science*, **367**, 171–175. doi: 10.1126/science.aaz0122.

[40] **Chen, Y. S., Haley, D., Gerstl, S. S. A., London, A. J., Sweeney, F., Wepf, R. A., …. Moody, M. P.** (2017). Direct observation of individual hydrogen atoms at trapping sites in a ferritic steel, *Science*, **355**, 1196–1199. doi: 10.1126/science.aal2418.

[41] **Mente, T., and Boellinghaus, T.** (2012). Modeling of Hydrogen Distribution in a Duplex Stainless Steel, *Weld. World.*, **56**.

[42] **Turnbull, A., and Hutchings, R. B.** (1994). Analysis of hydrogen atom transport in a two-phase alloy, *Mater. Sci. Eng. A.*, **177**, 161–171.

[43] **Sutton, M., Wolters, W., Peters, W., Ranson, W., and McNeill, S.** (1983). Determination of displacements using an improved digital correlation method, *Image Vis. Comput.*, **1**, 133–139.

[44] **Weidner, A., and Biermann, H.** (2021). Review on Strain Localization Phenomena Studied by High-Resolution Digital Image Correlation, *Adv. Eng. Mater.*, **23**.

[45] **Muniandy, K.** (2019). Digital image correlation for strain measurement in plastic film blowing process, *Mater. Sci. Technol.*, **35**, 1016–1027.

[46] **Lu, H., and Cary, P. D.** (2000). Deformation measurements by digital image correlation: Implementation of a second-order displacement gradient, *Exp. Mech.*, **40**, 393–400.

[47] **Yan, D., Tasan, C. C., and Raabe, D.** (2015). High resolution in situ mapping of microstrain and microstructure evolution reveals damage resistance criteria in dual phase steels, *Acta Mater.*, **96**, 399–409.

[48] **Örnek, C., Şeşen, B. M., and Ürgen, M. K.** (2022). Understanding Hydrogen-Induced Strain Localization in Super Duplex Stainless Steel Using Digital Image Correlation Technique, *Met. Mater. Int.*, **28**, 475–486.

[49] **Örnek, C., Larsson, A., Harlow, G. S., Zhang, F., Kroll, R., Carlà, F., …. Pan, J.** (2020). Time-resolved grazing-incidence X-ray diffraction measurement to understand the effect of hydrogen on surface strain development in super duplex stainless steel, *Scr. Mater.*, **187**, 63–67. doi: 10.1016/j.scriptamat.2020.05.061.

[50] **Lin, M., Yu, H., Ding, Y., Wang, G., Olden, V., Alvaro, A., …. Zhang, Z.** (2022). A predictive model unifying hydrogen enhanced plasticity and decohesion, *Scr. Mater.*, **215**. doi: 10.1016/j.scriptamat.2022.114707.

CURRICULUM VITAE

Name SURNAME **:** Bilgehan Murat ŞEŞEN

EDUCATION **:**

- **B.Sc.** **:** 2020, Istanbul Technical University, Faculty of Chemical Metallurgical Engineering, Department of Metallurgical and Materials Engineering
- **M.Sc.** **:** 2022, Istanbul Technical University, Graduate School, Department of Materials Science and Engineering

PROFESSIONAL EXPERIENCE AND REWARDS:

- 2020 - 2022 TUBITAK Scholarship Student, International Fellowship for Outstanding Researcher – 2232, Project No: 118C227
- 2020 Third Ranked Student in the Departmen of Metallurgical and Materials Engineering at ITU

PUBLICATIONS, PRESENTATIONS AND PATENTS ON THE THESIS:

- Örnek C, Müller T, **Şeşen BM**, Kivisäkk U, Zhang F, Långberg M, Lienert U, Jeromin A, Keller TF, Lundgren E and Pan J (2022) Hydrogen-Induced Micro-Strain Evolution in Super Duplex Stainless Steel—Correlative High-Energy X-Ray Diffraction, Electron Backscattered Diffraction, and Digital Image Correlation. Front. Mater. 8:793120. doi: 10.3389/fmats.2021.793120.
- Örnek, C., **Şeşen, B.M.** & Ürgen, M.K. Understanding Hydrogen-Induced Strain Localization in Super Duplex Stainless Steel Using Digital Image Correlation Technique. Met. Mater. Int. (2021). doi: 10.1007/s12540-021-01123-2.